Precision-porous biomaterials for skin healing

Meghan Wyatt

A dissertation
submitted in partial fulfillment of the
requirements for the degree of

Doctor of Philosophy

University of Washington
2024

Reading Committee:
Buddy D Ratner, Chair
Jonathan MD Himmelfarb
Miqin Zhang

Program Authorized to Offer Degree:
Bioengineering

University of Washington

Abstract

Precision-porous biomaterials for skin healing

Meghan Wyatt

Chair of the Supervisory Committee:
Buddy D Ratner
Department of Bioengineering

Current percutaneous devices often fail due to poor implant integration associated with the foreign body response (FBR). It is hypothesized that 40μm precision-porous biomaterials can inhibit the FBR to percutaneous devices. We investigated both synthetic and natural materials as potential candidates for precision-porous percutaneous device materials. Precision-porous polyurethane (PU) models of a catheter cuff were studied *in vivo* in a pig model. These PU constructs demonstrated a reduced FBR and better skin healing outcomes than solid implants. Subcutaneous implant models of precision-porous PU further demonstrated the ability of these materials to mitigate the FBR and improve angiogenesis. Analysis of RNA expression in subcutaneous models provided potential insights on the mechanism behind this pro-healing response. In the final component of this work, we investigated biodegradable biomaterials for use in percutaneous healing applications. Non-toxic, biodegradable PUs were developed.

Table of Contents

List of Figures

List of Tables

Chapter 1. SUMMARY AND SPECIFIC AIMS

More than 6 million Americans have chronic kidney disease with almost 55,000 dying of this condition each year[1]. Current hemodialysis treatment options negatively impact patient quality of life, hence the need for innovations. Innovations to hemodialysis treatment such as a wearable artificial kidney would require a robust percutaneous access mode that prevents infection and reduces risk of accidental device removal. However, healing of skin around biomedical devices at the percutaneous interface is compromised by the foreign body response (FBR) to implanted devices. The FBR occurs when proteins adsorbed on the biomaterial surface recruits macrophages and other monocytes. These macrophages in turn signal to fibroblasts which deposit excess collagen that separates the biomaterial from the rest of the body[2]. At the percutaneous interface, this lack of integration between biomaterial and tissue can lead to device failure[3]. It is hypothesized that limiting the FBR will lead to better outcomes for percutaneous devices as seen by improved tissue integration, increased vascularization, and reduced foreign body capsule (FBC). In addition to hemodialysis access, percutaneously implanted materials are utilized in osseo-integrated implants, burn treatments, long-term intubation, and catheters, among others[4]. Thus, improvements to percutaneous device healing would be of benefit to many applications.

The goal of the proposed work is to inhibit the extent of the FBR at the percutaneous interface. Research for this work investigates the following:

1.1 AIM 1: DEVELOP A CATHETER CUFF TO MINIMIZE THE FOREIGN BODY RESPONSE AT THE PERCUTANEOUS INTERFACE BY UTILIZING PRECISION-POROUS BIOMATERIALS

1.1.1 Aim 1.1: Synthesize precision porous biomaterials

In this work both polyurethane (PU) and gelatin-based precision-porous biomaterials were investigated as potential materials for a percutaneous catheter cuff. The ability for these scaffolds to support seeding with adipose-derived mesenchymal stem cells (aMSCs) was also tested. Both precision-porous biomaterials and stem-cell seeded biomaterials have shown promise in skin healing applications[5–10]. To confirm porous structure of materials and the attachment of stem cells we visualized the biomaterials via scanning electron microscopy (SEM).

1.1.2 Aim 1.2: *In vivo* studies of skin healing in mouse model

PU and gelatin-Dacron precision-porous biomaterials with and without aMSCs were implanted in the skin of mice. The utility of these materials for skin healing and their effect on the FBR was examined via histology.

1.1.3 Aim 1.3: *In vivo* study of catheter cuff in pig model

A model of the catheter cuff consisting of precision-porous PU surrounding a solid central rod was implanted intradermally in pigs. Infection resistance of these materials was examined via

bacterial challenge with methicillin-resistant *Staphylococcus aureus*. Mechanical strength was evaluated with Instron testing and FBR was evaluated with histology.

Innovation
Previous works have examined precision-porous biomaterials for skin healing[5,6]. However, no works have yet evaluated PU or degradable materials such as gelatin. Furthermore, the use of stem cell seeded aMSCs has yet to be examined. Additionally, previous work has only been performed on mouse models, whereas pig models provide a more reliable test due to their similarity to human skin properties and healing mechanism[11].

Impact
The use of precision-porous biomaterials to combat percutaneous device infection and lack of integration has potential utility in hemodialysis and other clinical applications such as burn treatment, osseo-integrated implants, long-term intubation, and long-term catheters among others.

1.2 AIM 2: INVESTIGATE THE DIFFERENCES IN IMMUNE RESPONSE TO IMPLANTS OF DIFFERING PORE SIZE

1.2.1 Aim 2.1: Examine effect of porosity on RNA expression of inflammatory markers

PU biomaterials were implanted subcutaneously in mice for 4 weeks then surrounding tissues were analyzed using NanoString nCounter inflammation panel to determine differences in gene expression.

1.2.2 Aim 2.2: Examine effect of porosity on FBR

PU biomaterials were implanted subcutaneously in mice for 4 weeks. Implants were evaluated via histology to determine vascularity, macrophage polarization, and collagen fibrosis.

Innovation
While prior works have documented the ability of 40μm precision-porous biomaterials to inhibit the FBR[12–15] the cellular mechanisms behind this phenomena remains unclear. We hypothesize that differential expression of inflammatory markers in response to porous biomaterials impacts the resulting FBR.

Impact
Polarization of macrophages to an M2 as opposed to M1 phenotype is generally associated with prevention of the FBR[16]. However, previous studies of 40μm precision-porous have shown a predominantly M1 response in material pores[12,17]. Detailed study of the inflammatory response could elucidate the underpinning of this apparent contradiction. An improved understanding of the mechanisms that underlie the ability of 40μm precision-porous biomaterials to inhibit the FBR could facilitate targeted engineering of further improved biomedical implants.

1.3 AIM 3: DEVELOP A BIODEGRADABLE SYNTHETIC MATERIAL FOR USE IN SKIN HEALING APPLICATIONS

1.3.1 Aim 3.1: Develop and characterize biodegradable synthetic material

A synthetic biomaterial that is elastic, soft, and degradable will be developed. Novel polyurethanes will incorporate either poly(lactic-co-glycolic acid) (PLGA) or polycaprolactone (PCL) as the degradable component.

1.3.2 Aim 3.2: Fabricate precision-porous biomaterial from degradable polymer

The synthetic polymer developed in Aim 3.1 will be optimized for creation of a degradable precision-porous scaffold. This will involve tuning of polymer component ratios and porous scaffold fabrication method to achieve uniform pore structure.

Innovation

Synthetic polymers often have more easily tunable mechanical properties and degradation rates than natural polymers[18]. Development of a biodegradable synthetic polymer that can be used in precision-porous biomaterial applications would allow these materials to be used in wound healing applications (such as burn-treatment) where tissue regeneration is the goal.

Impact

A biodegradable synthetic precision-porous biomaterial may have uses in clinical applications other than wound healing such as drug delivery.

Chapter 2. INTRODUCTION

2.1 The Problem: Complications of Percutaneous Devices

The skin provides a barrier to the outside world. It protects internal tissues by maintaining moisture and ion balance, resisting mechanical stress and providing a barrier to pathogen entry. However, in the context of medical care, it is often necessary to use percutaneous devices (such as a catheters), which by definition breach the skin barrier, to gain access to internal tissues. This breach can lead to a variety of complications. Failure of percutaneous devices is primarily caused by lack of integration[3]. In general, percutaneous devices poorly integrate with the skin which can cause inflammation, infection, and implant migration[3].

Infections of percutaneous devices are common. Two-thirds of patients with percutaneous osteointegrated devices experience infection[19]. While some infections are superficial, other percutaneous device-related infections can progress to serious systemic infections when bacteria from the skin surface migrate along the device and into the body[20,21]. This is especially common when implants undergo "marsupialization." In marsupialization, the epithelium grows down along the percutaneous implant creating a pocket between the device and the body which can harbor bacteria(Fig. 1)[3]. Poor integration at the device-skin interface provides an optimal surface for the formation of biofilms which can lead to persistent recurrent infections[22].

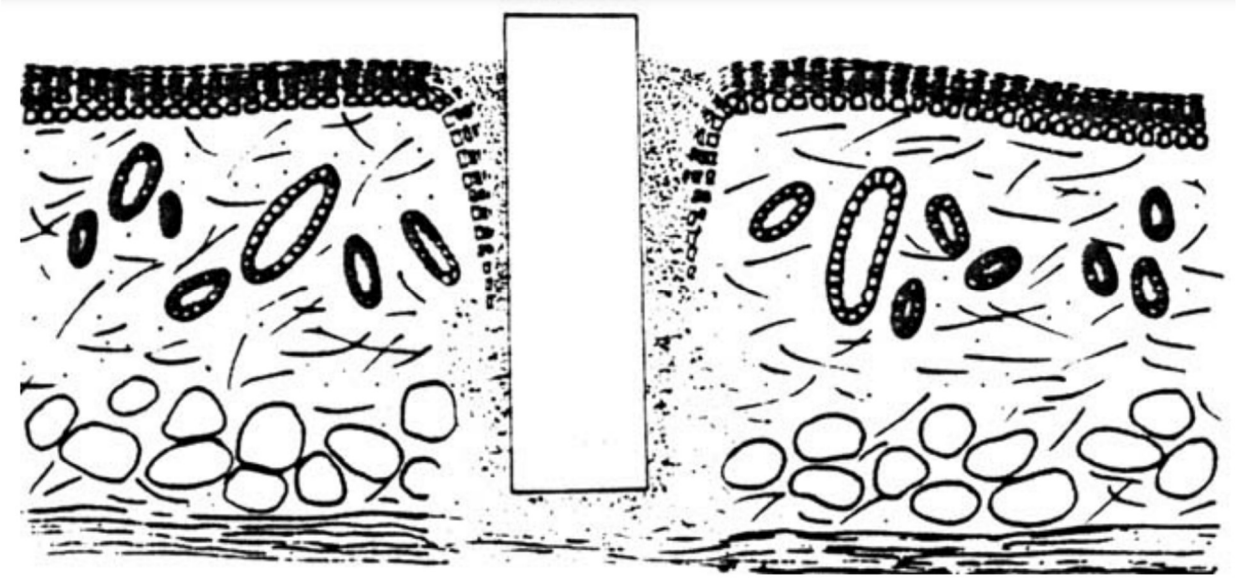

Figure 1. Schematic illustration of the marsupialization process. The epithelium (black) grows downward along the sides of the implant creating a pocket between the implant and body. Reproduced from Von Recum[3].

2.2 Background

2.2.1 Application of Percutaneous Devices: Hemodialysis

As of 2021, renal disease is one of the top ten causes of death in the United States[23]. While end stage renal disease can only be cured with kidney transplantation, hemodialysis can serve as a temporary replacement for kidney function. However, hemodialysis treatment negatively impacts patient quality of life. Additionally, innovations in hemodialysis treatment are rare and seldom of benefit to patients in terms of both treatment satisfaction and overall treatment survival[24]. It is vital that future innovations in the field of hemodialysis treatment improve both patient quality of life and clinical outcomes.

One proposed innovation to hemodialysis is a wearable artificial kidney. Such a device would require a continuous connection between the blood stream and the device, which necessitates a percutaneous catheter. Since this catheter would be directly connected to the vascular system long term, it is essential that it is infection-resistant and mechanically robust (to prevent accidental removal).

2.2.2 Foreign Body Response (adapted from my contributions to "Biocompatibility Evolves: Phenomenology to Toxicology to Regeneration" by *Crawford et al.*)

The implantation of biomaterials causes injury to the body's tissues which initiates a nonspecific host immune response known as the foreign body reaction (FBR)[25]. The acute phase of the FBR is similar to natural wound healing, however the characteristics of biomaterials, even those considered biocompatible, often lead to chronic inflammation. In response to injury, local blood vessels increase in permeability, and platelets accumulate and aggregate at the injury site. The aggregation of platelets is coupled with the release of cytokines and other factors that attract neutrophils to the site in the acute inflammation phase[2,26]. Next, mononuclear cells migrate to the site and remain at the biomaterial-tissue interface during the chronic inflammation phase[2,26]. The persistent inflammatory stimulus that is the implanted biomaterial causes these interfacial mononuclear cells to eventually fuse into multinucleated foreign body giant cells (FBGCs). Finally, fibrosis occurs as granulation tissue forms around the implant[2,26–28].The FBR can lead to poor implant outcomes and, in some cases, failure of implanted biomedical devices[2,27,29,30].

The FBR can be broken down into 5 sequential phases: (i) protein adsorption, (ii) acute inflammation, (iii) chronic inflammation, (iv) foreign body giant cell formation, and (v) fibrous encapsulation. These phases are summarized in Figure 2. The FBR is initiated when proteins adsorb on the surface of a biomaterial[2,26,27,31,32]. Following protein adsorption, neutrophils infiltrate the implantation site. Activated neutrophils degranulate at the biomaterials surface, releasing inflammatory mediators that recruit more leukocytes and monocytes to the site[25]. In the chronic inflammation stage of the FBR, monocytes infiltrate the biomaterial site. Over time, monocytes fuse into foreign body giant cells (FBGCs). With regard to the FBR to biomaterials, FBGCs are large, multinucleated cells formed by fusion of macrophages after frustrated phagocytosis of an implant[2,33,34]. FBGCs are found at the implant surface and can mediate device degradation and failure over time[35]. Finally, the biomaterial is encapsulated in acellular, fibrotic capsule composed predominantly of collagen 1[26,36] that has several deleterious implant outcomes including: deformation and mechanical stress of the biomaterial via fibrotic contraction[37]; separation from the surrounding tissues which can lead to failure of devices dependent on tissue interaction[27,30];

poor vascularization of the capsule and surrounding tissue and increased infection risk[26,38]. In this work precision-porous biomaterials are utilized in order to mitigate the FBR and improve biomaterial integration.

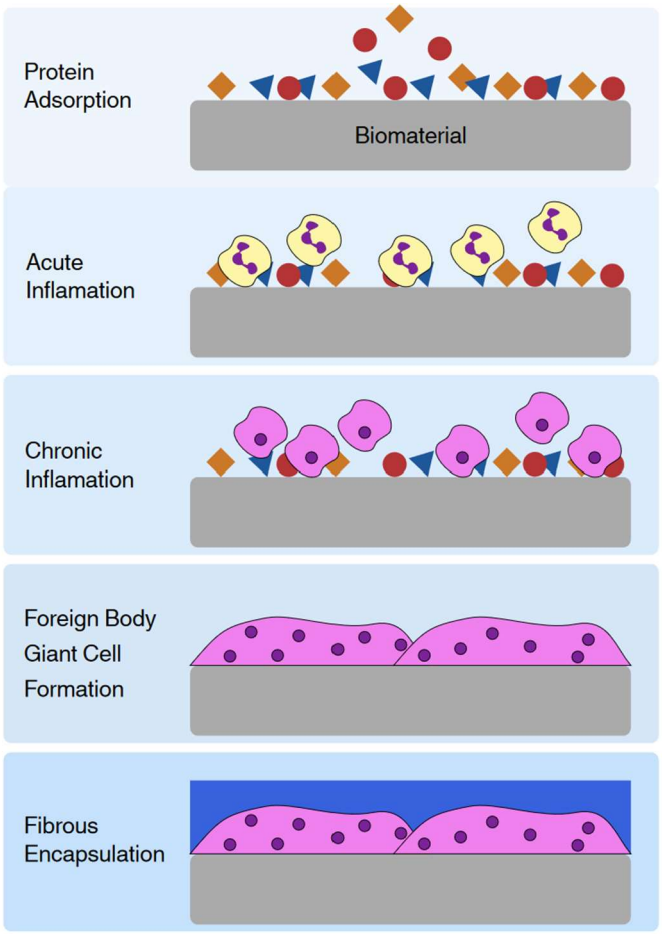

Figure 2. Phases of the foreign body reaction. Proteins (including fibrinogen, albumin and complement proteins) adsorb to the biomaterial upon implantation. During acute inflammation neutrophils, shown in yellow, accumulate at the implantation site. In chronic inflammation macrophages, shown in pink, are attracted to the implantation site. Macrophages fuse into foreign body giant cells following frustrated phagocytosis. Finally, the biomaterial is encapsulated by fibrous tissue, shown in blue[39].

2.2.3 Macrophage Polarization

Macrophages are cells of the monocytic lineage whose primary function is phagocytosis. Activated macrophages express a variety of different markers and can direct the activity of other immune cells[39]. Macrophage activation exists on a spectrum ranging from M1 or "Classically activated" macrophages to M2 or "Alternatively activated" macrophages. M1 macrophages secrete pro-inflammatory cytokines and long-term persistence of M1 polarization is associated with chronic inflammation and autoimmune diseases[40]. M2 macrophages secrete anti-inflammatory cytokines and are associated with immunosuppression and wound healing[41]. In the field of biomaterials, M1 macrophages are broadly associated with the FBR and poor healing outcomes, while M2 macrophages are associated with tissue modelling and regeneration.

However, the inflammation process is more nuanced. It is thought that an early shift in macrophage phenotype (i.e. M1 polarization predominant at the beginning stages of healing and M2 polarization predominant at later stages) is optimal for achieving best biocompatibility and tissue integration[16].

2.2.4 Precision-Porous Biomaterials

Precision-porous biomaterials are constructs formed from pores with a uniform size and uniform interconnect size. Prior works have shown that biomaterials fabricated to have a 40μm pore size with ~13μm interconnects promote tissue integration and vascular ingrowth while mitigating the FBR[12–15]. Biomaterials with larger or smaller pore sizes do not mitigate the FBR to the same extent[38]. Previous studies have shown favorable outcomes in regards to skin integration into these materials[5,6]. Notably, precision-porous biomaterials promote both epidermal and dermal ingrowth and avoid marsupialization of implants[6]. This is important for infection prevention at the percutaneous interface. Precision-porous biomaterials can be made from a wide variety of materials both natural and synthetic such as poly-(2-hydroxyethyl methacrylate), silicone, fibrin, polyurethane (PU), and gelatin[6,12,14,42]. The diversity of materials available for use in precision-porous scaffolds enhances their adaptability to specific applications.

2.2.5 Biodegradable Biomaterials

Relative to conventional, non-degradable biomaterials, biodegradable biomaterials possess the advantage of being resorbed into the body after they have served their intended purpose. They are widely used in the field of tissue engineering as scaffolds for drug delivery, cell seeding, and tissue regeneration[18]. Biodegradable biomaterials can be made of either natural or synthetic materials, or a combination of both. Synthetic biomaterials often have a higher mechanical strength than natural materials, while natural materials can possess inherent growth factors and cell signaling sites[18,43,44]. Biodegradable materials have been widely studied in the field of skin regeneration. FDA approved commercial products made from collagen, elastin, fibrin, and hyaluronic acid are on the market. Other materials including gelatin, poly (lactic-co-glycolic acid) (PLGA), polycaprolactone (PCL), and polyurethane (PU) among others are being investigated in the literature[43].

2.2.6 Stem Cells for Skin Healing

Stem cells are multipotent cells capable of self renewal[45]. Mesenchymal stem cells (MSCs) are a type of stem cell present in adult tissues. MSCs can be isolated from many tissues such as bone marrow, adipose tissue, nerve tissue, and cutaneous tissue[46]. Their ease of isolation as compared to other types of stem cells makes them an attractive choice for regenerative medicine applications. In wound healing MSCs have demonstrated the capacity to enhance angiogenesis, recruit endogenous progenitor cells, and speed wound healing through the production of growth factors and immunomodulatory factors[46,47]. Previous studies have shown that MSCs enhance healing in cutaneous wounds[7–10]. MSCs can be seeded onto biomaterials for both ease of delivery to the injury site and improvement of biomaterial modulated healing[7,48].

2.3 The Project: Biomaterials for Improved Skin Healing

It is hypothesized that an elimination or reduction of the FBR at the percutaneous interface of biomedical implants would reduce infection risk in long-term implants. Further, integration of regenerated skin and implant would allow for greater mechanical strength and reduce chances of implant removal and migration. For a wearable artificial kidney device, an infection resistant and mechanically robust connection to the bloodstream is essential, thus a percutaneous implant that mitigates the FBR is needed. In this work, precision-porous biomaterials composed of non-degradable PU or of Dacron mesh and gelatin were investigated as potential components of a percutaneous catheter cuff for application in a wearable artificial kidney system (Fig 3). Since percutaneous devices can be used for a wide variety applications in addition to hemodialysis access, this work also focuses on the development of a synthetic degradable polymer that can be used in skin healing.

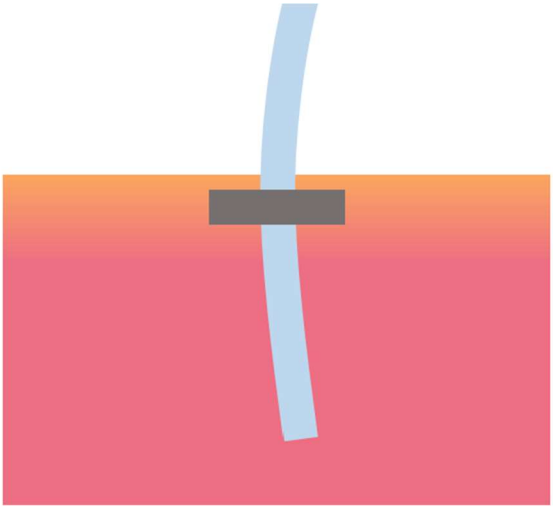

Figure 3. Percutaneous interface cuff (grey) surrounding a venous access catheter (blue). The cuff provides mechanical support and infection prevention by healing directly into the skin.

Chapter 3. CREATE A CATHETER CUFF TO MINIMIZE THE FOREIGN BODY RESPONSE AT THE PERCUTANEOUS INTERFACE BY UTILIZING PRECISION-POROUS BIOMATERIALS

3.1 Abstract

Precision-porous biomaterials have been investigated in this work as a method of mitigating the FBR to implanted biomaterials. It is hypothesized that 40μm precision-porous biomaterials will be effective in decreasing FBR around percutaneous implants. It is also hypothesized that aMSCs can further mitigate the FBR. Precision-porous biomaterials were fabricated from both synthetic (PU) and natural (gelatin-Dacron) biomaterials. Materials both with and without aMSCs were tested in mouse models of skin healing. PU materials were further tested in a pig model of a percutaneous catheter cuff to better capitulate the human skin healing response. PU 40μm precision-porous biomaterials demonstrated decreased FBC formation and better implant-tissue integration than control solid implants.

3.2 Materials and Methods

3.2.1 Materials

Poly (tetramethylene oxide) (PTMO, commercial name: PolyTHF® 1000) (585788) was purchased from BASF Corporation. 4,4′-Methylenebis (phenyl isocyanate) (MDI) (256439), 1,1,1-tris (hydroxymethyl) propane (TMP) (93370), N-hydroxysuccinimide (NHS) (130672), Masson's trichrome stains (HT15), Bouin's solution (HT10132), Harris hematoxylin solution (HHS32), eosin Y solution (HT110332), Formalin solution, neutral buffered 10% (HT501128), gelatin from porcine skin (Type A) (G1890) and collagenase type I (SCR103) were purchased from Sigma-Aldrich. Dulbecco's modified eagle medium (DMEM) (11995-065) and antibiotic penicillin streptomycin (15140–122) were purchased from Gibco. 25 cm^2 cell culture flasks were purchased from Corning Incorporated. 1,3,5-tris (6-isocyanatohexyl) biuret (HTI, commercial name: Desmodur N3200) (5288673) was purchased from Bayer Material Science. N-(3-dimethylaminopropyl)-N'-ethyl carbodiimide (EDC) (3450) was purchased from Fluka. Uncrosslinked, monodisperse 40 μm poly (methyl methacrylate) (PMMA) microspheres were purchased from MICROBEADS (Norway). Polyester Mesh (Dacron) (PETKM2004) was purchased from Textile Development Associates. Methylene chloride (DCM) (D143-4), acetone (A949-4), methanol (A452-4), and Permount® mounting Medium (SP15-100) were purchased from Fisher Scientific. Anhydrous ethanol (64-17-5) was purchased from Decon Labs. Superfrost Plus glass Slides (71869–10) were purchased from Electron Microscopy Sciences. Integra bilayer wound dressing was purchased from Integra LifeSciences.

3.2.2 Fabrication of PU implants

The PU used in this work has a Young's Modulus of 432 ± 23 kPa[14] which falls within the range of the Young's Modulus values of native skin (420 to 850 kPa)[49].To create a precision-porous scaffold template, PMMA microspheres (40μm) were poured into molds created by sandwiching a Teflon spacer between two glass slides. Molds were sonicated for one hour to allow for close

packing of the PMMA spheres. After sonication, the molds were sintered for 24 hours at 175°C to create uniform pore-interconnects of ~13µm. The PU was prepared by mixing PTMO preheated to 80°C with TMP at 100°C for 15 minutes. This mixture was then placed under −30 inch Hg vacuum at 80°C for one hour to remove water before mixing with HTI and MDI. The molar ratio of PTMO/MDI/HTI/TMP was 4/3/4/4. The PU mixture was pipetted into the Teflon-PMMA molds and subjected to -25 inch Hg vacuum for 5 minutes to ensure complete infiltration of the molds by the polymer solution. The vacuum was purged with nitrogen. This process was repeated two times. Molds were then placed in an oven at 80°C for 48 hours to complete polymerization. After polymerization, the non-porous PU surface layer was scraped off using a razor blade. PMMA templates were removed using three 24 hour washes in DCM with continuous agitation, followed by a 24 hour wash in acetone with continuous agitation, seven 24 hour washes in 100% EtOH with continuous agitation, and then a gradual hydration to DI water. Circular implants 6mm in diameter were cut using a biopsy punch.

3.2.3 Fabrication of gelatin-Dacron implants

Broadly the fabrication of gelatin-Dacron implants follows a similar process to fabrication of PU implants with the following key changes: Prior to filling the mold with PMMA beads, a Dacron mesh was inserted between the glass slides and Teflon spacer (Fig 4). Sonication and sintering were performed as in 3.2.2. Mold infiltration was completed as in 3.2.2 using a 10% gelatin solution in place of the PU. Molds were refrigerated overnight then cross-linked using EDC and NHS at a ratio of 1:0.2 EDC:NHS and 1:4 EDC:carboxylic acid (COOH)[50]. COOH amount was calculated using the average COOH acid content of type A gelatin (78 mmols per 100 grams). After crosslinking, the surface layer was scraped and removal of the PMMA template proceeded as in 3.2.2.

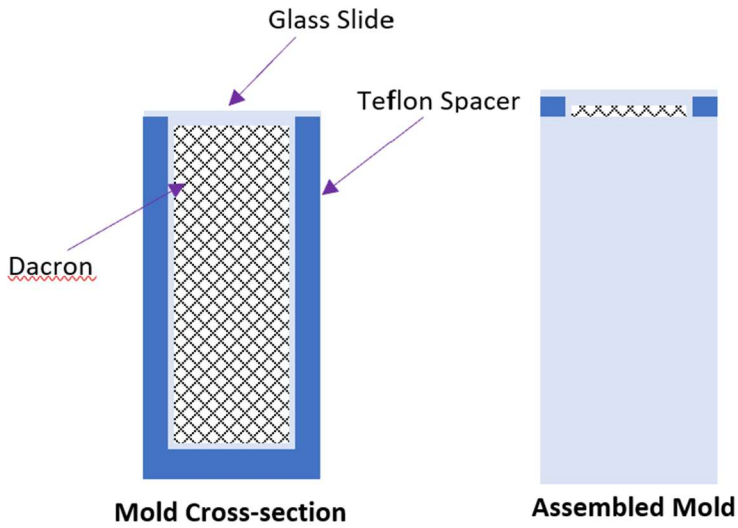

Figure 4. Illustration of the Dacron-mesh mold construction

3.2.4 Fabrication of PU rod implant

PMMA templates were fabricated as 3.2.2 with the addition of 4mm Teflon spacers to leave space for a solid central rod. Following polymerization, the spacers were removed and Teflon tubing was used as a mold for a solid central rod of the same PU composition. After polymerization of the central rod, scraping and PMMA removal proceeded as in 3.2.2. Implants were cut into 2 cm diameter circles, with the 4mm rod at the center. Rods were trimmed to protrude between 4-5mm above the implant. Implant thickness was 0.8mm. Implants were sterilized by autoclave at 259°F at a max pressure of 17.9 psi for 45 minutes.

3.2.5 Adipose-derived stem cell isolation and seeding

Adipose-derived mesenchymal stem cells (aMSCs) were isolated from mouse adipose tissue following the procedure described by Zomer[10]. Briefly, fat tissues were mechanically degraded then incubated in a DMEM solution with 1% collagenase 1 for 1 hour at 37°C. Collagenase activity was blocked with fetal bovine serum and the tissue digest was filtered through a 70µm sieve and centrifuged for 5 minutes at 300g. Cells were suspended and plated with DMEM containing 10% fetal bovine serum, 1% glutamine, and 0.5% penicillin-streptomycin.

To determine cell-viability on precision-porous implants, aMSCs were seeded on PU scaffolds and tissue culture polystyrene using a direct pipetting technique. A WST-1 assay for cell proliferation was performed. Seeded scaffolds were also imaged with SEM to confirm cell adherence.

3.2.6 Scanning Electron Microscopy (SEM)

The structure of porous scaffolds and attachment of aMSCs to scaffolds were imaged using a SNE-3200M SEM machine by SEC Co. Samples were sputter coated with Au/Pt using a MCM-200 ion sputter coater at 6 mA for 60 s, 3 repetitions. aMCS seeded scaffolds were prepared for SEM using critical point drying to preserve cell structure.

3.2.7 Intradermal implantation studies in mice

All animal experiments were approved by the University of Washington Animal Care and Use Committee (IACUC) and carried out in accordance with the National Institutes of Health guide for the care and use of laboratory animals. Both male and female C57BL/6 mice were used to account for differences in skin healing between sexes[51]. Animals were between 4-6 months old and had a body weight of greater than 22 g. Mice were anesthetized with isoflurane. A 200 µl injection of buprenorphine was given to each mouse at the dose of 0.05 mg/kg body weight to reduce pain. All implants were assessed for endotoxicity and cytotoxicity following protocols described in ISO 10993-5. Two *in vivo* mouse models were studied for this work. In the first model, after shaving and disinfection, a 6mm biopsy punch was used to remove sections of skin from the right and left sides of the upper back. Disc shaped implants 6mm in diameter and of 0.8mm thickness of 40µm precision-porous PU or Integra(control group) either with or without aMSCs (Table 1) were inserted into the wound.

Table 1. Implant groups for first intradermal implant study

Implant	n
Integra(control)	6
Integra + cells	6
PU	6
PU + cells	6

Implants were covered with Tegaderm to prevent water loss and secured with sutures. In the second model, a 4mm biopsy punch was used to remove sections of skin from the right and left sides of the upper back. Disc shaped implants 6mm in diameter and of 0.8mm thickness were inserted into the wound (Table 2). Wounds were covered with Tegaderm secured by skin glue. Visual healing of implants was documented by photography at 0, 3, 7, 14, and 21 days post implantation. At 21 days mice were euthanized and implants explanted.

Table 2. Implant groups for second intradermal implant study

Implant	n
Integra(control	3
Integra + cells	3
PU	6
PU + cells	6
Gelatin-Dacron	6
Gelatin-Dacron + cells	6
Dacron (control)	3
No implant (control)	3

3.2.8 Implant harvesting and processing

Mice were euthanized using CO2 asphyxiation followed by cervical dislocation. The upper back of each mouse was thoroughly shaved. Implants were excised and fixed in zinc fixative for 24–48 hours at room temperature with gentle agitation. All tissues were processed using conventional histochemical techniques, embedded in paraffin wax and 5-µm sections were mounted on glass slides, deparaffinized and stained with routine stains to evaluate wound-healing phases, as described below.

3.2.9 Qualitative assessment of inflammation

Samples were stained with hemotoxylin and eosin staining (H&E). Qualitative assessment of inflammation was performed by a blinded pathologist. Masson’s trichrome staining was used to

examine foreign body capsule (FBC) formation. Images were taken with an optical microscope (Nikon E800).

3.2.10 *In vivo* model of catheter cuff

All animal experiments were approved by the University of Washington Animal Care and Use Committee (IACUC) and carried out in accordance with the National Institutes of Health guide for the care and use of laboratory animals. Two female Yuctan mini-pigs were used in this study. Each pig received 8 dorsal implants (Fig 5).

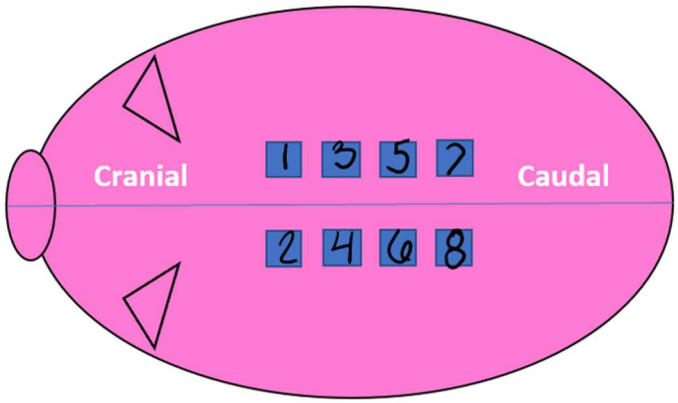

Implant Site	Implant Type	Concept
1	Porous	General Healing
2	Porous	
3	Porous	Instron
4	Porous	
5	Porous	Bacterial Challenge
6	Porous	
7	Solid	
8	Solid	

Figure 5. Diagram of implant placement and type for in vivo pig model

Implants were designed to mimic the catheter cuff design intended for use in hemodialysis access. Solid implants were included as a control. All implants were assessed for endotoxicity and cytotoxicity following protocols described in ISO 10993-5. Pigs received anesthesia and analgesia for surgical procedures. Implantations were performed by creating a flap in the dermis and creating a hole though the epidermal side of the flap. Implants were inserted beneath the flap with the implant rod protruding through the hole (Fig 6). Immediately prior to implant surgery and under anesthesia, a baseline blood draw was taken for a CBC. Following surgery, animals received weekly blood draws for CBCs and monitoring blood for potential bacteremia. After the implant surgery, the site was dressed with sterile gauze and a protective, breathable jacket was worn by the animal full time for the first 7 days of the healing process. Dressing changes were performed twice during the initial week post-surgery and once weekly during the remainder of the experiment. The implants sites were photographed at each dressing change to monitor the healing progression of the implant sites.

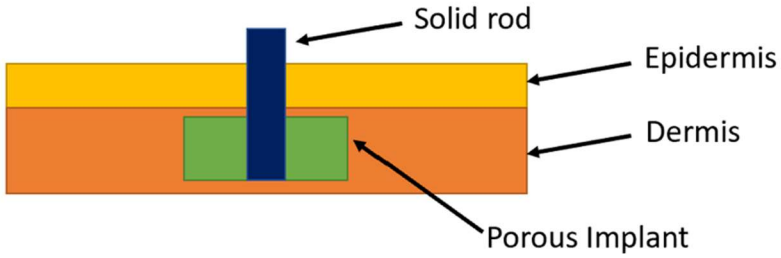

Figure 6. Intradermally implanted catheter cuff model. A solid center rod protrudes through the epidermis, while the main, porous, portion of the implant rests in the dermis.

3.2.11 Bacterial challenge

After 26 days, implant sites 5, 6, 7, and 8 underwent a bacterial challenge procedure (Fig 5). Gauze soaked in methicillin resistant *Staphylococcus aureus* (MRSA) was applied to the implant site for 48 hours. 10^6 colony forming units were applied to each implant site. After 48 hours the gauze was removed. Animals were monitored for signs of infection during the challenge and for the 3 days following. Following implant harvest and fixation, bacterial challenge sites were stained with a Gram stain following the method detailed by Brown and Hopps to check for the presence of bacteria on the biomaterial and in the surrounding tissue[52].

3.2.12 Implant harvesting and processing

Animals were euthanized via injection 32 days post implant surgery. Explanted tissue sections from sites 1, 2, 5, 6, 7, and 8 (Fig 5) were fixed in 10% formalin for 48 hours at room temperature[53]. Tissues were processed using conventional histochemical techniques, embedded in paraffin wax, and 5-µm sections were mounted on glass slides, deparaffinized and stained with routine stains to evaluate wound-healing phases, as described below. Explanted tissue sections from sites 3 and 4 were kept on ice and evaluated for mechanical strength as described in the following section.

3.2.13 Tensile strength testing

Tensile properties were measured using a 5540 Series Single Column System Instron testing machine (Instron, Norwood, MA) with a 500 N load cell. Materials were punched using a dog-bone shaped steel blade dimensioned per ASTM D-1708-96-MET standard. The Bluehill Materials Testing (Instron) software was used to collect data from the tests. The samples were stretched at a constant rate of 10 mm/min. Young's modulus was calculated from the stress strain curve. Normal pig skin harvested at the same time as the implants was used as a control.

3.2.14 Histological assessment of skin healing and FBR

Tissue sections were stained with H&E for qualitative assessment of skin healing. Measurements of the foreign body capsule (FBC) thickness around the implants were also taken from Masson's trichrome stained sections. Samples were imaged on a Nikon E800 microscope. Three measurements were taken from random sections of each implant at 10X magnification using ImageJ.

3.2.15 Data analysis and statistics

For comparisons of multiple groups two-way ANOVA with Bonferroni correction was used to determine statistical significance. A p value (after Bonferroni correction) less than 0.05 is considered statistically significant. For comparisons of two groups student's t-test was used.

3.3 Results and Discussion

3.3.1 Precision-porous structure

SEM imaging revealed a uniform, orderly, and interconnected pore structure in PU implants. Gelatin-Dacron implants showed expanded and diffuse pores. However, this is likely due to the lyophilization process required for SEM imaging. Since gelatin is a hydrogel, the water loss impacts the structure seen under SEM. Dacron fibers are incorporated into the structure cross-section of the gelatin scaffold (Fig 7).

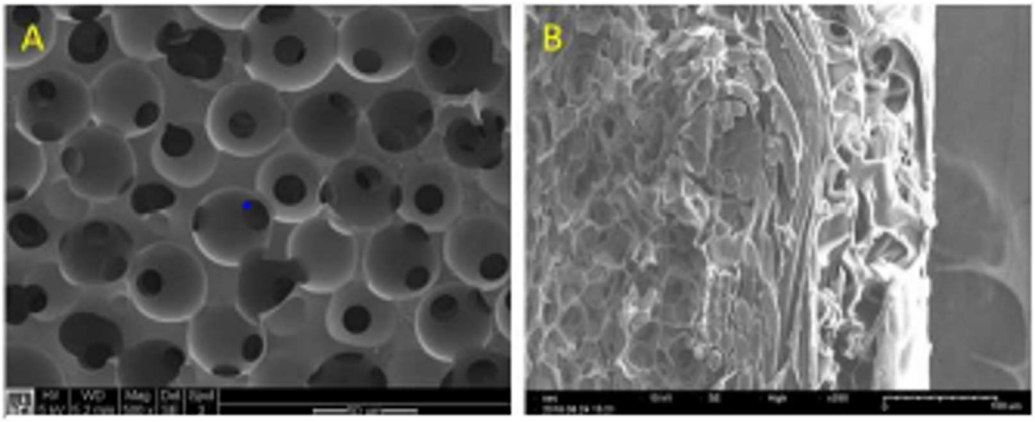

Figure 7. SEM of porous structure A) PU implant, B) gelatin-Dacron implant. Pore structure of gelatin is slightly altered due to dehydration

3.3.2 aMSC viability

aMSCs seeded on precision-porous PU scaffolds had similar survival rates to aMSCs seeded on tissue culture polystyrene as measured by WST-1 cell proliferation assay (Fig 8). Measurements were taken at 1, 3, and 7 days. Increased absorbance is indicative of increased cell numbers. The increase in absorbance from day 1 to day 7 indicates that the cells can proliferate in the PU scaffold environment.

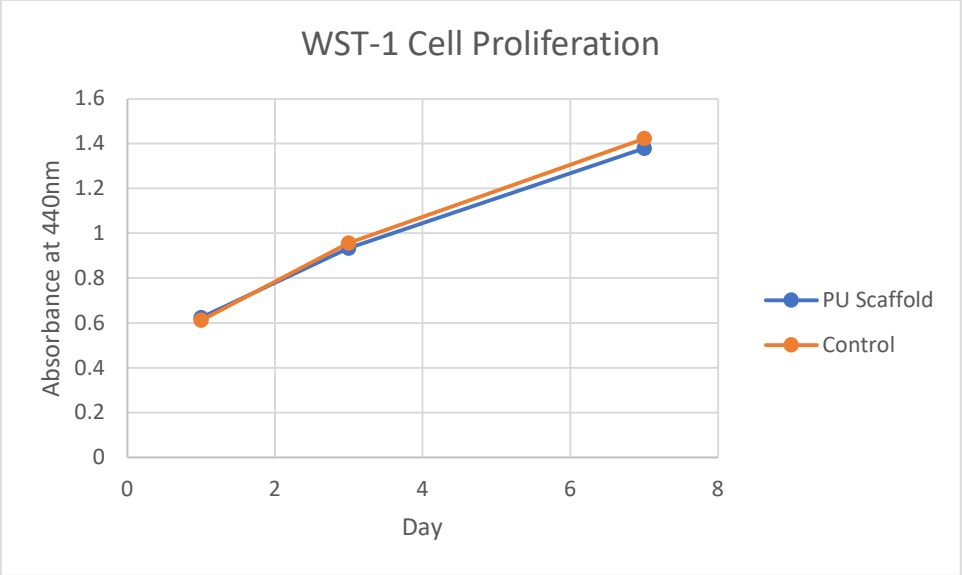

Figure 8. Adipose derived mesenchymal stem cell proliferation

SEM imaging showed that aMSCs were able to adhere to the PU scaffold material and infiltrate the pores (Fig 9). After 48 hours cells had infiltrated 220 µm into the scaffolds. The adherence of cells and proliferation of cells on the precision-porous PU material demonstrates that it is an adequate scaffold for aMSCs.

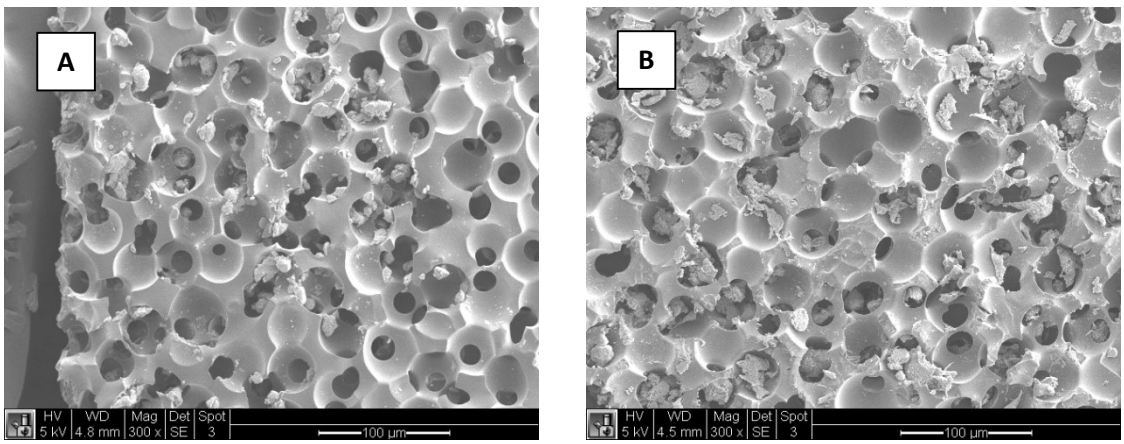

Figure 9. SEM image of aMSCs on PU A) Scaffold cross-section with aMSC infiltration, B) Scaffold surface with aMSC adherence

3.3.3 Clinical evaluation of healing

For the first mouse study of intradermal implantation, healing was evaluated clinically 7 days post surgery. Implant color was graded to be pink, yellow, or pale (no associated color). Pink coloring of implants is an indication of angiogenesis in the wound bed, while yellow coloring can be indicative of infection. In the control group (Integra, FDA approved skin substitute) all of the implants were pale. Both the PU and PU + aMSC group had four pink implants. The PU + aMSC also had one pale implant and one yellow implant. Integra + aMSCs had three pink implants, one yellow implant, and two pale implants. Due to the mice removing implant sutures, three of the implants fell out before the 7 day time point and were excluded from analysis. Initial interpretation of these results supports the conclusion that both aMSCs and precision-porous PU can improve angiogenesis, which can indicate better regenerative outcomes. Unfortunately, the study was terminated early since the mice were able to remove the majority of the implants. The implant surgical procedure was modified for the subsequent study to prevent this outcome.

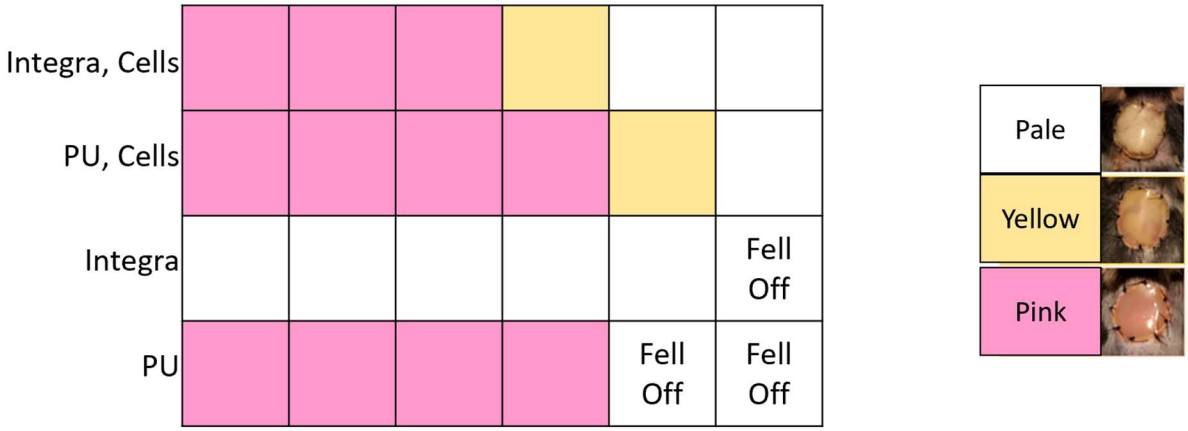

Figure 10. Clinical evaluation of wound color at 7 days post-implantation

3.3.4 Inflammatory response to implants in mice and FBC formation

Inflammation associated with intradermal implants of PU, PU + aMSCs, Integra (control), Integra + aMSCs, gelatin-Dacron, gelatin-Dacron + aMSCs, Dacron (control) and no implant (control) was evaluated by a blinded pathologist. Inflammation was scored on the following scale: 0:no inflammation, 1:minimal inflammation, 2:mild inflammation, 3:moderate inflammation, 4:severe inflammation. During the course of the second intradermal implantation model, one mouse perished due to unknown causes and one mouse was euthanized due to infection. Both animals received one PU implant and one PU implant with aMSCs. The implants were not harvested, resulting in an n of 4 for each of those groups. Semi-quantitative scoring revealed a significant difference in inflammation between animals treated with Dacron and animals receiving no implant ($p=0.00423$). No significance was found between other treatment groups. However, animals treated with gelatin-Dacron both with and without aMSCs showed higher levels of inflammation. Since Dacron is known to be inflammatory this finding is not surprising.

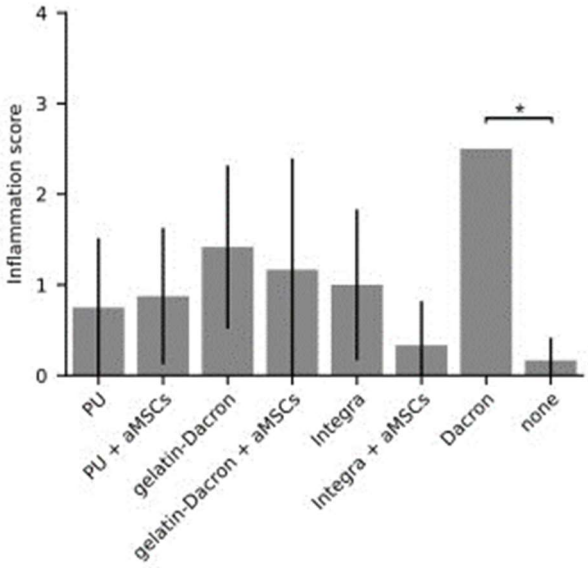

*Figure 11. Semi-quantitative inflammation scoring of implants. Error bars represent standard deviation, * indicates significance of $p<0.05$*

Masson's trichrome staining revealed the lack of a dense FBC surrounding PU and gelatin-Dacron 40µm precision-porous implants both with and without aMSCs (Fig 12). This is inline with previous investigations of 40µm precision-porous biomaterials which demonstrate that these materials mitigate the FBR[12–15]. Staining also revealed that the implants had migrated subcutaneously instead of staying in the dermis. Mouse skin is very thin which makes implantation and securing of implants intradermally difficult. Further, rodent skin has a layer of muscle underneath which contracts during the healing process[54]. This can also lead to implant migration. We concluded that a mouse model was not optimal for exploring healing of intradermal implants.

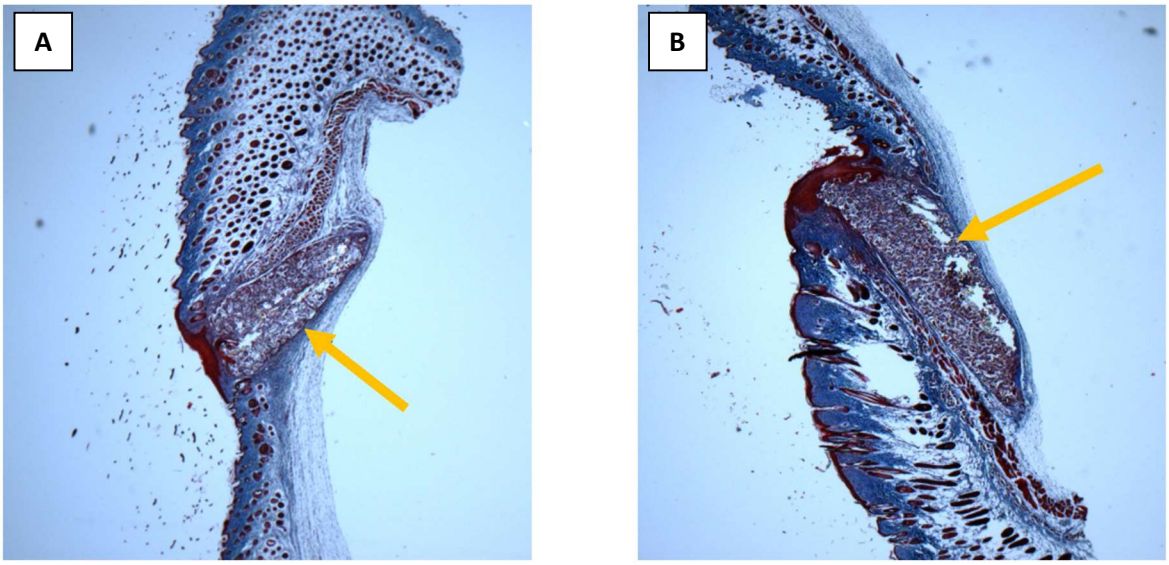

Figure 12.Trichrome images of implants A) PU, B) gelatin-Dacron. implants (right) are marked with arrows. Both implants (yellow arrows) show cellular infiltration of pores (red) and lack of dense collagen capsule.

3.3.5 Clinical evaluation of healing in pigs

For modeling percutaneous implantation of a catheter cuff a pig model was chosen. Clinical observations of healing found extrusion of one solid implant and mild necrosis surrounding the rod portion of two additional solid implants. Porous implants appeared normal on visual inspection (Fig 13). No signs of infection (redness, swelling, warmth) were observed at any of the implant sites. While there was no visible infection, it is possible that bacteria on implants are present in levels that did not cause symptoms prior to euthanasia. Further histological analysis of the bacterial load on implants is necessary.

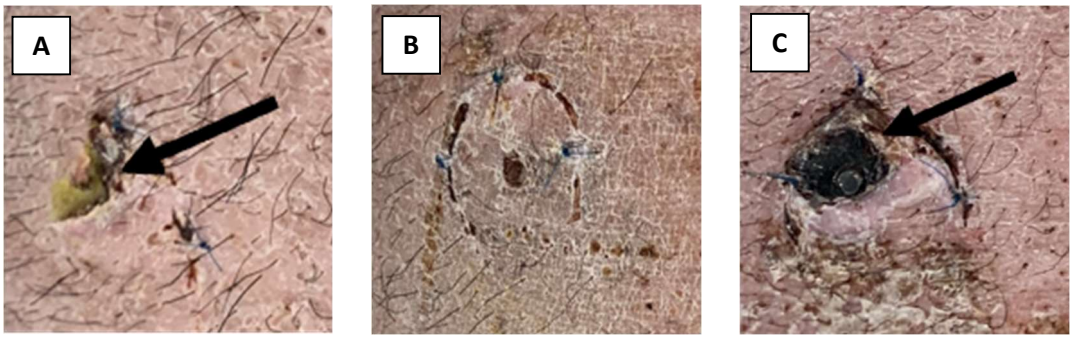

Figure 13. Implant site healing at 32 days post surgery. A) Normal implant B) Extruding implant, C) necrosis

3.3.6 Mechanical strength

To test the robustness of the skin-implant integration, samples were tested for tensile strength (Fig 14). The Young's Modulus of native skin (860 kPa) was slightly-less than that of skin with implanted precision-porous PU (1070 kPa). This result can be interpreted to mean that the mechanical connection between the skin and the implant is robust and that the elasticity of the implant is well matched to that of skin.

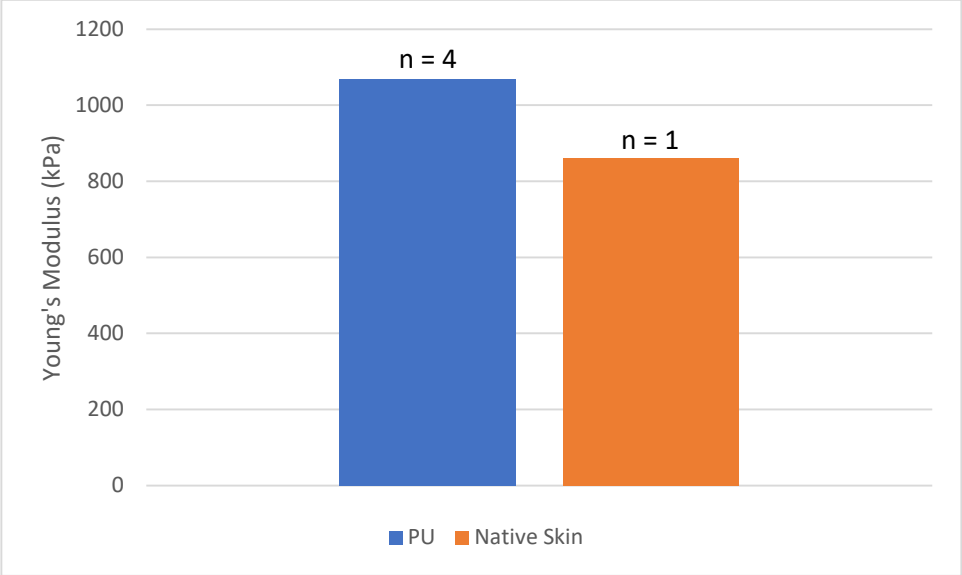

Figure 14. Tensile strength of skin with precision-porous PU implants

3.3.7 Histological evaluation of skin healing in pigs

A model of a percutaneous catheter cuff was created by encompassing a solid central rod with a disc either 40µm precision-porous PU or solid PU. H&E evaluation of the rod portion of the implant revealed marsupialization of the rod on solid implants vs skin growth flush with the rod on porous implants (Fig 15). This reduction of epidermal downgrowth at the implant site is advantageous, as it indicates better integration and infection-prevention potential. Masson's trichrome stains showed cellular ingrowth into the porous structure (Fig 17).

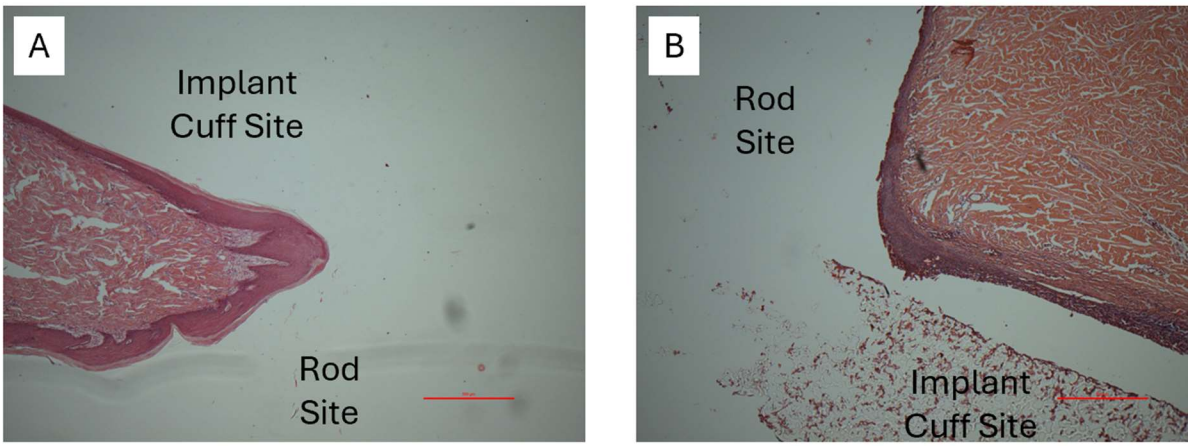

Figure 15. H&E staining of rod portion of implant at 4X magnification. A) solid PU implant, B) 40µm precision-porous PU implant

FBC measurements revealed thicker collagen capsules surrounding solid implants than porous implants ($p < 0.001$). Average thickness of FBC surrounding solid implants was 374 ± 46 µm compared to 138 ± 19 µm for porous implants (Fig 16). The FBC capsule for porous implants is thicker than the capsules measured in previous studies[12,13]. However, previous studies were performed in mouse models as opposed to pig models and utilized much smaller implant sizes. It is likely that differences in the healing of pig tissues as opposed to mouse tissues are responsible for the larger overall capsule sizes in both solid and porous implants. The FBC size was significantly smaller in porous implants highlighting the ability of 40µm porous scaffolds to mitigate the FBR. Further, examination of the FBC surrounding porous implants reveals a dense cellular component more akin to granulation tissue than the typical collagenous, acellular capsule (Fig 17).

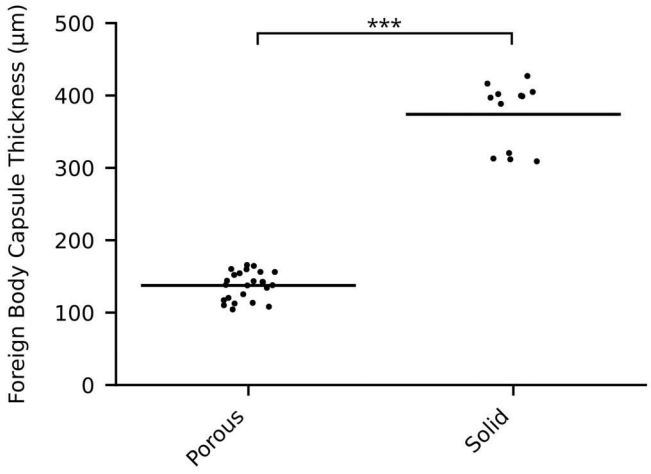

*Figure 16. Measurement of FBC thickness surrounding pig model implants, *** indicates $p<0.001$*

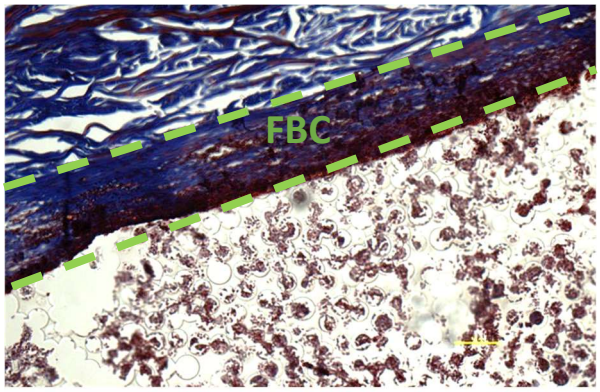

Figure 17. Cellular ingrowth and FBC cellular content of precision-porous PU implants

3.3.8 Histological evaluation of bacterial challenge

Gram staining of the implants revealed no evidence of bacteria on the implant surfaces of porous and solid implants or within the porous implants (Fig 18). It is possible that the bacterial dosage used in this test was not high enough to provide a relevant picture of infection risk.

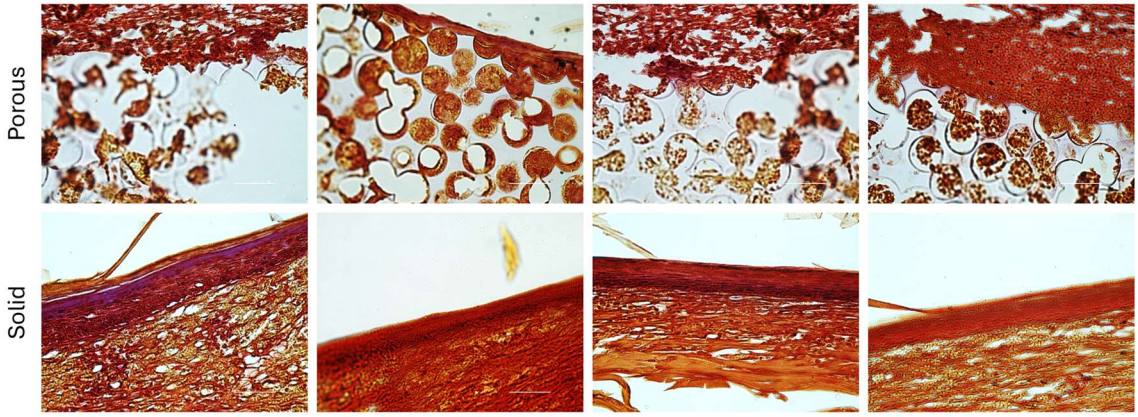

Figure 18. Gram stain of porous and solid implants

3.4 Conclusions

In summary, we evaluated a 40µm precision-porous PU biomaterial for use in percutaneous device applications. This material improves healing as seen by reduction in the FBC thickness, cellular integration into material pores, prevention of epidermal downgrowth, and lack of infection. Confirmation of these effects in a pig model, which best capitulates human skin, highlights the ability of this material to be used in percutaneous applications. We believe it to be an ideal candidate for use in wearable hemodialysis applications as a percutaneous catheter cuff as well as other implantable devices.

3.5 Acknowledgements

I would to acknowledge Le Zhen, PhD for his mentorship and design of the PU formulation used in this work. Sharon Creason has provided laboratory mentorship and designed the

animal use protocol as well as performed the mouse surgeries. Helena Zomer provided mentorship on the mouse study design and pathology interpretation. Elina Quiroga performed the pig surgeries. Prof. Jessica Snyder provided analysis of implant pathology. David Yang assisted with troubleshooting the histology process. I would like to acknowledge Prof. Buddy Ratner for the design of the project and mentorship. Generous funding for this work was provided by a grant from the Northwest Kidney Centers to the University of Washington Center for Dialysis Innovation (CDI).

Chapter 4. INVESTIGATE THE DIFFERENCES IN IMMUNE RESPONSE TO IMPLANTS OF DIFFERING PORE SIZE

4.1 Abstract

Biomaterials that integrate into the body and improve healing response are expected to have better outcomes upon implantation. In this work we fabricated precision-porous PU scaffolds with 40μm pores. We hypothesize that these scaffolds will improve healing, promote angiogenesis, and mitigate the FBR. To test this hypothesis 40μm precision-porous, 100μm precision-porous, and solid PU materials were implanted subcutaneously in mice. Differences in gene expression of the cells associated with each implant were analyzed to potentially elucidate the mechanism behind different healing responses. FBC thickness and vascularization of implants were also measured. Results show that 40μm porous materials exhibit the least amount of FBC formation and the most vascularization, suggesting that they are ideal for a wide range of biomaterial applications. Potential differences in gene expression at the implant-tissue interface were also noted.

4.2 Materials and Methods

4.2.1 Materials

Poly (tetramethylene oxide) (PTMO, commercial name: PolyTHF® 1000) (585788) was purchased from BASF Corporation. 4,4′-Methylenebis (phenyl isocyanate) (MDI) (256439), 1,1,1-tris (hydroxymethyl) propane (TMP) (93370), Masson's trichrome stains (HT15), Bouin's solution (HT10132), Harris hematoxylin solution (HHS32), and eosin Y solution (HT110332) were purchased from Sigma-Aldrich. 1,3,5-tris (6-isocyanatohexyl) biuret (HTI, commercial name: Desmodur N3200) (5288673) was purchased from Bayer Material Science. Uncrosslinked, monodisperse 110μm and 40μm poly (methyl methacrylate) (PMMA) microspheres were purchased from MICROBEADS (Norway). Methylene chloride (DCM) (D143-4), acetone (A949-4), methanol (A452-4), and Permount® mounting Medium (SP15-100) were purchased from Fisher Scientific. Anhydrous ethanol (64-17-5) was purchased from Decon Labs. Superfrost Plus glass Slides (71869–10) were purchased from Electron Microscopy Sciences. Anti-CD31 rabbit polyclonal antibody (ab124432) was purchased from Abcam. Impress-AP horse anti-rabbit IgG (MP-5401), Vector blue substrate kit (SK-5300), VectaMount aqueous mounting medium (H-5501), and Bloxall (SP-6000) were purchased from Vector Labs

4.2.2 Fabrication of PU implants

PU implants of three different structures were used in this work: 40μm precision-porous, 100μm precision-porous, and solid (no pores). 40μm precision porous PU implants were fabricated as described in 3.2.2. 100μm were fabricated as described in 3.2.2, using 100μm PMMA microspheres and a temperature of 177°C for 19.5 hours for the sintering process. This is the optimal time and temperature to achieve pores with interconnects of about one third total pore size (~33 μm). Solid PU implants were fabricated by mixing PU components as described in 3.2.2 then polymerizing in molds composed of a Teflon spacer between two glass slides. Porous structure of implants of confirmed with SEM.

4.2.3 Subcutaneous implantation studies in mice

All animal experiments were approved by the University of Washington Animal Care and Use Committee (IACUC) and carried out in accordance with the National Institutes of Health guide for the care and use of laboratory animals. Both male C57BL/6 mice were used. Mice were anesthetized with isoflurane. A 200 µl injection of buprenorphine was given to each mouse at the dose of 0.05 mg/kg body weight to reduce pain. All implants were assessed for endotoxicity and cytotoxicity following protocols described in ISO 10993-5. After shaving and disinfection disc shaped implants 6mm in diameter and of 0.4 mm thickness of 40µm precision-porous PU, 100µm precision-porous PU, or solid PU were inserted into the left and right subcutaneous space of the upper back. Each mouse received two of the same implant type, since half of the implants were used for NanoString analysis and half of the implants were processed for conventional histology. After 4 weeks mice were euthanized and implants explanted.

4.2.4 Implant harvesting and processing

Mice were euthanized using CO2 asphyxiation followed by cervical dislocation. The upper back of each mouse was thoroughly shaved. Left and right implants of each mouse were randomly designated to be processed for NanoString analysis or conventional histology. For NanoString analysis, care was taken to excise the implant while including minimal extra tissue from the surrounding regions, since we wanted to focus analysis on cells in the FBC region. Implants were placed in sterile PBS and placed on ice. For conventional histology, implants were excised and fixed in zinc fixative for 24–48 hours at room temperature with gentle agitation. All tissues were processed using conventional histochemical techniques, embedded in paraffin wax and 5-µm sections were mounted on glass slides, deparaffinized and stained with routine stains to evaluate wound-healing phases, as described below.

4.2.5 NanoString analysis

Explanted tissues were sent to Fred Hutchinson Cancer Center for RNA extraction and nCounter processing. Samples were evaluated using the NanoString Fibrosis panel which measures expression levels of genes related to inflammation, cell proliferation, and the immune system. For the panel, color-coded oligonucleotide probes bind with the sample RNA. These probes are immobilized on a slide and counted by the nCounter system. Analysis of RNA expression levels was performed in nSolver Analysis software version 4.0. Expression levels were normalized using 10 “housekeeping genes”, *i.e.* genes that are not expected to show variance in expression levels across experimental conditions. Background noise was removed utilizing negative control thresholding. The fold change between expression of each gene was calculated between each group. Statistical significance was calculated via student’s *t*-test. A Benjamini-Yekutieli correction was applied to account for multiple comparisons[55] with significance defined at the $\alpha=0.05$ level.. As an additional, exploratory analysis, genes of interest were identified as those with lowest p-values prior to Benjamini-Yekutieli correction, in particular, $p<0.01$. Principle component analysis was also performed on the gene expression data to determine if expression differences could be correlated between multiple genes.

4.2.6 Quantitative measurement of FBC

Measurements of the foreign body capsule (FBC) thickness around the implants were also taken using Masson's trichrome stain to identify the FBC. Samples were imaged on a Nikon E800 microscope. Three measurements were taken from random sections of each implant at 10X magnification using imageJ.

4.2.7 Analysis of endothelial cells in pores

Immunohistochemistry was performed for the endothelial cell marker CD31 in order to visualize blood vessels in explanted tissue. Briefly, rehydrated tissue sections were incubated in tris-buffered saline (TBS) prior to antigen retrieval. Heat-mediated antigen retrieval was performed using EDTA buffer solution. Following antigen retrieval slides were washed in TBS with 0.1% Tween 20. Endogenous alkaline phosphatase activity was blocked by incubation slides in Bloxall for 20 minute. Non-specific protein absorption was blocked by incubating slides in 2.5% normal horse serum for 30 min. CD31 antibody was diluted 1:50 in 2.5% normal horse serum TBS solution with 0.1% Tween. Slides were incubated overnight at 4°C then washed with TBS. Slides were incubated with ImmPress horse-anti-rabbit reagent for 30 min and then washed with TBS. Vector blue substrate was added and slides were monitored until color developed after which they were washed and mounted. Imaging was done on a Nikon E800 microscope. Using ImageJ images were converted to greyscale. Regions of interest were identified as the capsule surrounding the implant for solid, 40µm, and 100µm implants and as the area inside the pores for 40µm and 100µm implants. Three random fields were selected from each sample. Thresholding of the color values allowed for identification and measurement of the percentage of positively stained tissue in each area.

4.2.8 Data analysis and statistics

Statistics on RNA expression ratios were performed as described in 4.2.5. For other comparisons a student's *t*-test was used with $p < 0.05$ considered significant.

4.3 Results and Discussion

4.3.1 NanoString gene expression

RNA expression differences between each pair of samples (40µm precision-porous vs 100µm precision-porous, 40µm precision-porous vs solid, and 100µm precision-porous vs solid) were calculated in nSolver. Numerous genes appeared to have differing expression between groups. However, these high-throughput assays entail thousands of statistical comparisons, necessiting multiple comparisons correction to ensure the false discovery rate remains low. After applying a correction for multiple comparisons (Benjamini-Yekutieli correction) they fail to meet the significance threshold. Principle component analysis revealed no significant clustering of expression values by group (Fig 19). This suggests that either (i) gene expression remains largely similar regardless of implant type, or (ii) that the study is underpowered, a possibility supported by the small sample size (n=4). Another limitation of this study is that it is difficult to precisely isolate the FBC from surrounding healthy tissue, which could skew the results to make different sample groups appear more similar than they actually are.

While no genes demonstrated significantly different expression after multiple comparisons correction, we nonetheless performed additional exploratory analyses to better understand candidate genes that varied most between the implants. In particular, we sorted genes by lowest p-value (before correction) and considered the genes differentially expressed between each pair of implants with $p < 0.01$. Since we hypothesized that the mechanistic basis, in terms of gene expression, for the improved healing of the 40µm implants over the solid implants may match that which explains the improved healing of the 40µm implants over the 100µm implants, we then narrowed our search by selecting genes identified simultaneously by both of these analyses. Genes identified included Irak3 and Cyp2j6. Both were expressed less in the tissues associated with 40 µm implants than in the other groups.

Irak3 suppresses toll-like receptor signaling which results in decreased production of inflammatory cytokines[56]. Knockdown of Irak3 polarizes macrophages to an M1 phenotype thus this is suggestive of a higher proportion of M1 macrophages in the 40µm implants[57]. Similarly, Cyp2j6 expression is associated with inhibition of an M1 phenotype[58]. Cyp2j6 expression was lower in 40µm implants also suggesting a higher proportion of M1 macrophages in the 40µm implants. While on a surface level this result seems counterintuitive, since M2 macrophages are considered "pro-healing" and M1 macrophages are considered "pro-inflammatory," it speaks to a more nuanced view of inflammation rather than the broad categorization of M2 as favorable and M1 as unfavorable. M1 macrophages are known to promote angiogenesis, which is an essential component of healing[59]. 40µm precision-porous materials demonstrate a concentration of M1 macrophages within the pores and M2 macrophages on the surface[12]. Further, spatial confinement (such as within pores) can downregulate inflammatory cytokine production by M1 macrophages[60]. Further research is needed to clarify how the immunes response to 40µm precision-porous biomaterials leads to improved healing as defined by decreased FBC and increased angiogenesis.

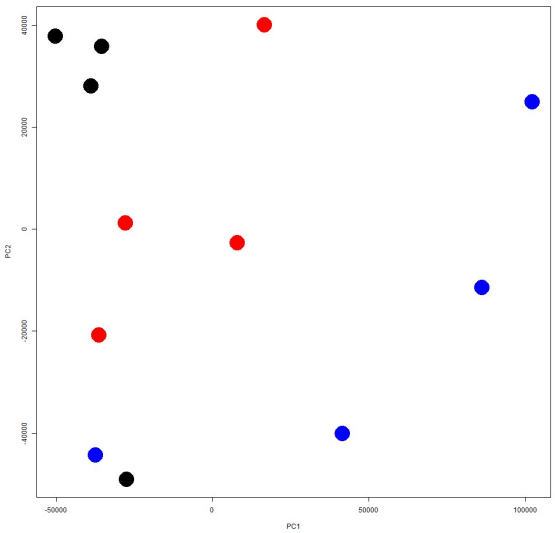

Figure 19. Principle component analysis of NanoString gene expression values. Black indicates solid implants, red indicates 40µm precision-porous implants, and blue indicates 100µm precision-porous implants.

4.3.2 FBC thickness measurements

The FBC surrounding solid implants was thicker than that of 40µm porous implants ($p < 0.001$). The FBC surrounding 100µm porous implants was also thicker than that of 40µm porous implants ($p<0.001$) Average thickness of FBC surrounding were 134 ± 38, 106 ± 36 µm, 30 ± 11 µm and f[illegible]lid, 100µm, and 40µm implants respectively (Fig 20). This confirms that 40µm precision-p[illegible]s biomaterials mitigate the FBR as compared to solid materials and that pore size is instrumental in achieving this effect.

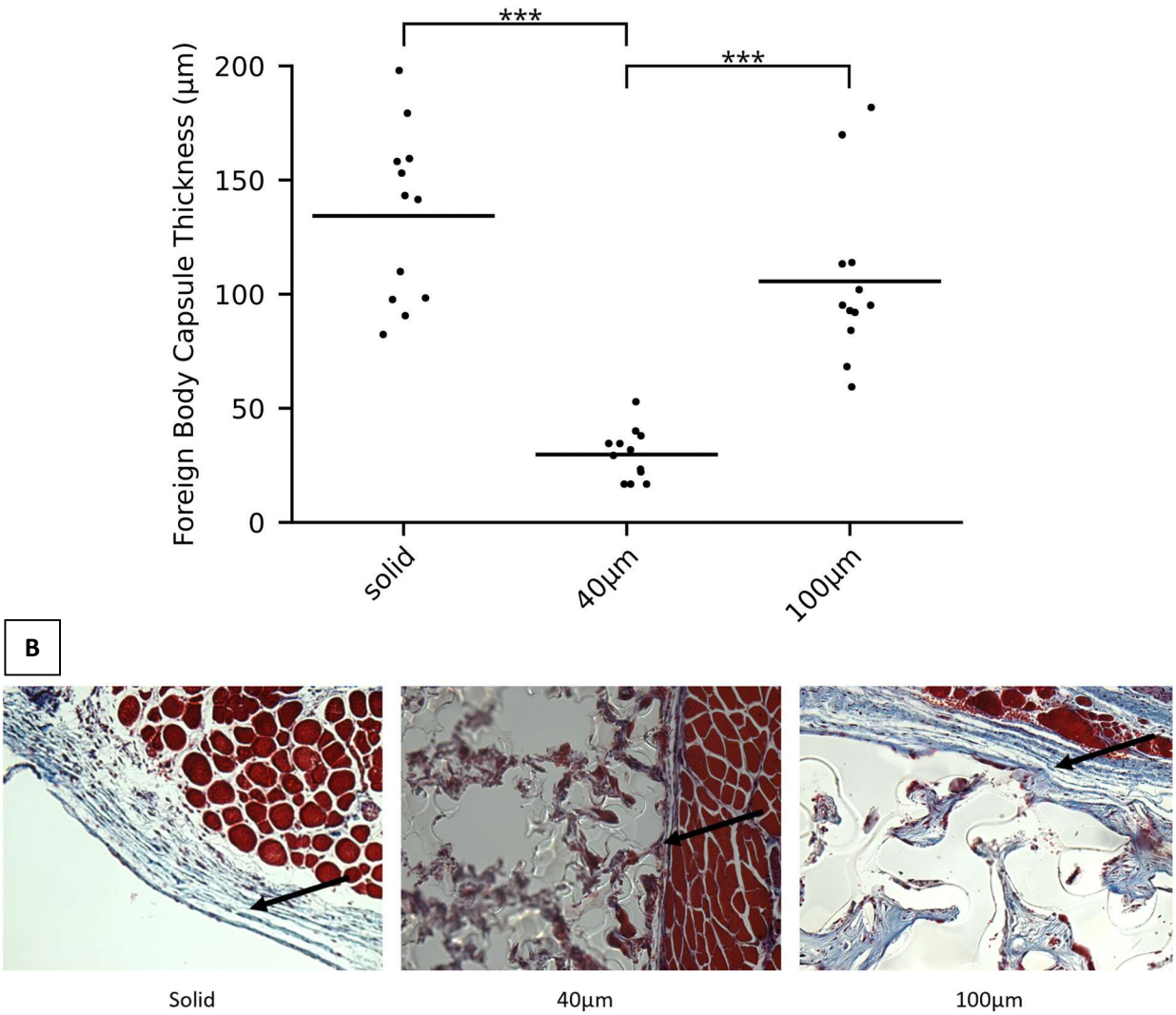

*Figure 20. FBC thickness surrounding subcutaneous implants, A)Quantitative measurements of capsule thickness, *** indicates p<0.001, B)Representative images of FBC (black arrows)*

4.3.3 Endothelial cells in pore structure

To examine angiogenesis in and around the implants, tissue sections were stained with endothelial cell marker CD31. Positive staining was observed in the pores of both 40µm precision-porous

implants and 100µm precision-porous implants, with positive staining more abundant in 40µm pores (Fig 21). The dense layer of FBC surrounding the solid implants and 100µm porous implants did not show evidence of endothelial cells. Average percentage of tissue staining positive for CD31 in the capsule region was 4.35±2.07 for solid implants, 19.29±6.35 for 40µm implants, and 16.47±6.21 for 100µm implants (Fig 22). There was a significant difference ($p<0.001$) between angiogenesis in the capsule region between solid implants and 40µm implants and between solid implants and 100µm implants. For the region inside the pores, 40µm implants had 25.91±8.66 percent positively stained area versus 17.99±4.74 for 100µm implants ($p>0.05$) (Fig 23).

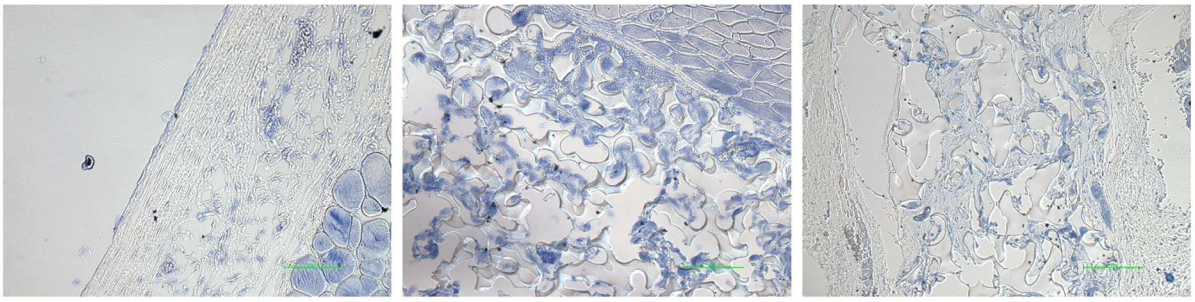

Figure 21. Immunohistochemical assessment of vascularization. Representative images are taken at 20X magnification

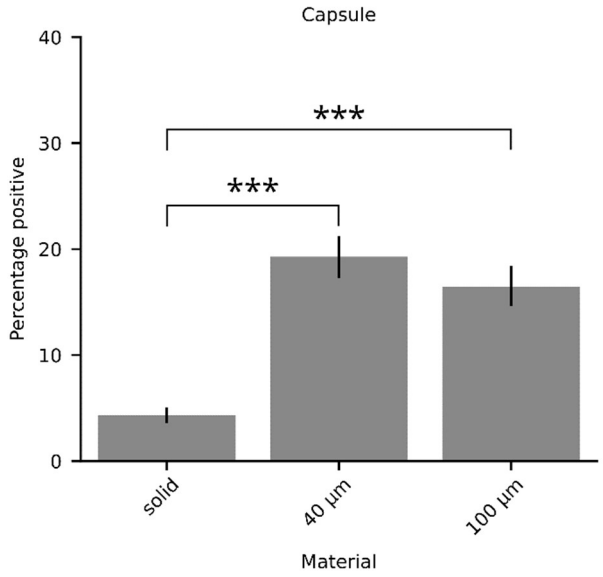

*Figure 22. Percentage of area positively stained for CD31 in capsule region, *** indicates $p<0.001$*

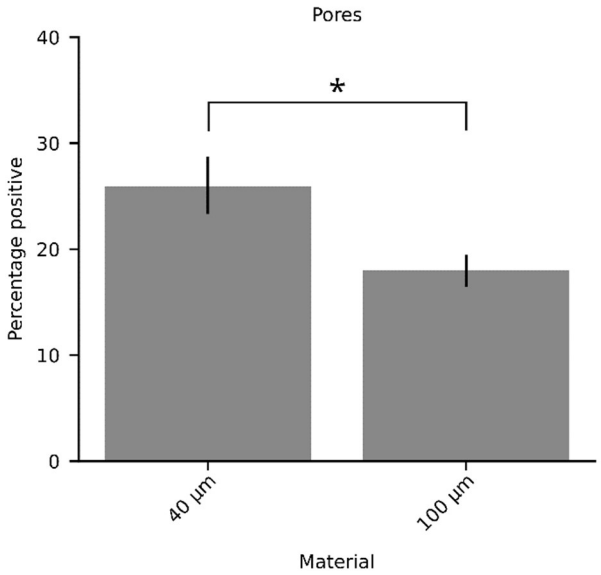

*Figure 23. Percentage of area positively stained for CD31 in pores, * indicates p<0.05*

4.4 Conclusions

In summary, we evaluated a 40µm precision-porous PU biomaterial to elucidate it's healing properties. This material improves healing as seem by reduction in the FBC thickness and improved angiogenesis. We believe it to be an ideal candidate for use in implantable device applications. Investigations of gene expression at the implant-tissue interface revealed potential upregulation of pro-inflammatory genes by the 40µm precision-porous PU. This supports the hypothesis that inflammation can be a driving force behind healing. We will investigate this further in future works through evaluations of macrophage marker expression.

4.5 Acknowledgements

I would to acknowledge Le Zhen, PhD for his design of the PU formulation used in this work. Sharon Creason has provided laboratory mentorship and designed the animal use protocol as well as performed the mouse surgeries. Louis Chen assisted with mouse surgeries. Pamela Yang performed the RNA extractions. Ian Stanaway, PhD assisted with principle component analysis. I would like to acknowledge Prof. Buddy Ratner for the design of the project and mentorship. Generous funding for this work was provided by a grant from the Northwest Kidney Centers to the University of Washington Center for Dialysis Innovation (CDI)

Chapter 5. DEVELOP A BIODEGRADABLE SYNTHETIC MATERIAL FOR USE IN SKIN HEALING APPLICATIONS

5.1 Abstract

Optimal materials for skin healing are biodegradable to guide the formation of healthy regenerated tissue. Synthetic degradable biomaterials offer advantages in the ability to easily tune mechanical properties and degradation rate for the desired application. In this work degradable PU materials containing PLGA or PCL as the degradable segment were formulated. Materials were tested for degradation kinetics and biocompatibility. PLGA-PU materials degraded in 6-10 weeks and were biocompatible. PCL biomaterials were also biocompatible and were suitable for precision-porous scaffold applications.

5.2 Materials and Methods

5.2.1 Materials

Poly(lactide-co-glycolide)-3-arm trimethylolpropane initiated (PLGA-TMP) (AP247) was purchased from Akinalytics. 1,4 butanediol (BD) (493732) and polycaprolactone diol (189405) were purchased from Sigma Aldrich. Dulbecco's modified eagle medium (DMEM) (11995-065) and antibiotic penicillin streptomycin (15140–122) were purchased from Gibco.

5.2.2 Synthesis of crosslinked PLGA PUs

Crosslinked PUs containing PLGA as a degradable component were synthesized in a catalyst-free, solvent-free process. PLGA-TMP was heated to 80°C. PLGA-TMP, BD, and LTI were mixed at 60°C for 10 minutes. The polymer mixture was then placed under −30 inch Hg vacuum at 55°C for 3 minutes. Vacuum was purged with nitrogen. Polymerization was completed overnight at 55°C under nitrogen.

5.2.3 *In vitro* degradation of PLGA PUs

PLGA PUs were placed in vials of PBS and kept at 37°C. At each timepoint (days 0, 1, 3, 7, 14, 21, 28, 42, 56, and 70) PBS was replaced and samples were lyophilized and weighed.

5.2.4 Degradation product toxicity of PLGA PUs

PLGA PU was incubated in DMEM at 37°C for one week. DMEM containing degradation products was combined with untreated DMEM at the following to create 1%, 10%, and 50% solutions. 3T3 fiberblasts were plated on tissue culture polystyrene and grown to ∼80% confluency before initiating the assays. After 48 hours, cell viability was measured with WST-1 assay. Results were normalized to the control group of cells grown in untreated DMEM.

5.2.5 Synthesis of crosslinked PCL PU

Crosslinked PUs containing PCL as a degradable component were synthesized in a catalyst-free, solvent-free process. PCL diol was heated to 80°C. PCL diol, BD, and LTI were mixed at 60°C for 10 minutes. The polymer mixture was then placed under −30 inch Hg vacuum at 55°C for 3

minutes. Vacuum was purged with nitrogen. Polymerization was completed overnight at 55°C under nitrogen.

5.2.6 Accelerated *In vitro* degradation of PCL PUs
PCL PUs were placed in vials of 5 M NaOH aqueous solution at room temperature. Samples were monitored to determine if complete degradation occurred.

5.2.7 Degradation product toxicity of PCL PUs
PCL PU was incubated in DMEM at 37°C for one week. DMEM containing degradation products was used as growth media for 3T3 fibroblasts following ISO10993 standards. Fibroblasts were plated on tissue culture polystyrene and grown to ~80% confluency before initiating the assays.

5.2.8 Fabrication of Porous PCL PU implants
Precision-porous scaffold molds were created as described in 3.2.2. PCL PU was prepared as described in 5.2.5. Mold infiltration by polymer and washing process were completed as described in 3.2.2.

5.2.9 Scanning Electron Microscopy (SEM)
The structure of porous scaffolds was imaged using a SNE-3200M SEM machine by SEC Co. Samples were sputter coated with Au/Pt using a MCM-200 ion sputter coater at 6 mA for 60 s, 3 repetitions.

5.3 Results and Discussion

5.3.1 PLGA PU synthesis

Optimal degradable polymers for use in skin healing applications should be soft, strong, and elastic. PLGA PUs consisting of PLGA-TMP, LTI, and BD were mixed in various ratios (Table 3).

Polymer Code	**PLGA-TMP/LTI/BD Molar Ratio**
dPU1	1/2/1.5
dPU2	1/2.5/2.25
dPU3	1.5/2/1.5
dPU4	1/2/2.75

Table 3. Chemical compositions of PLGA PUs

dPU1 was brittle and non-elastic. This formulation was excluded from further testing. dPU2, dPU3, and dPU4 underwent *in vitro* degradation studies.

5.3.2 PLGA PU *in vitro* degradation
Degradation was characterized by the percentage of mass lost over time. dPU2 degraded fully in about 8 weeks, dPU3 degraded fully in about 4 weeks, and dPU4 degraded fully in about 10

weeks (Fig 24). *In vitro* characterization of degradation does not fully capitulate degradation *in vivo*, as materials in the body are exposed to a more complex degradation environment that includes degradation enzymes and cells, as such *in vivo* degradation times are often faster than *in vitro*.

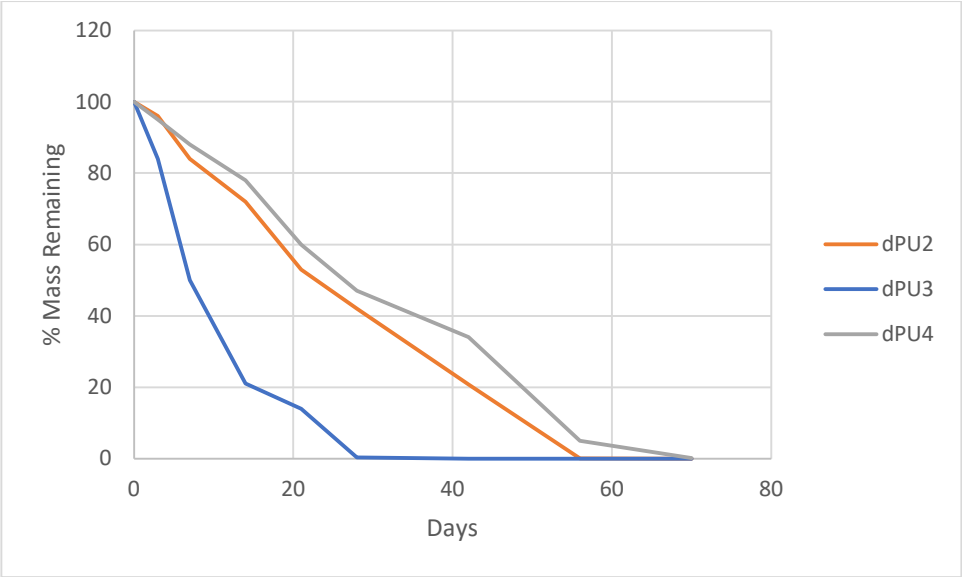

Figure 24. Degradation of PLGA-PU in vitro

5.3.3 PLGA PU degradation product toxicity

Degradation products of dPU2, dPU3, and dPU 4 were found to be non-toxic (Fig 25). Cell viability as measured by WST-1 assay was similar to viability in controls.

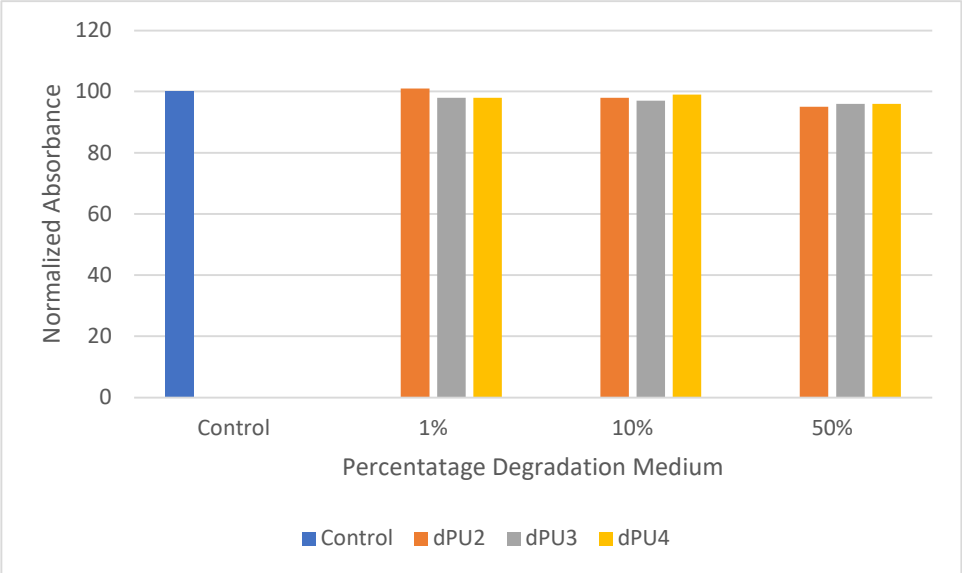

Figure 25. WST-1 cell viability of 3T3 fibroblasts cultured with PLGA-PU degradation products

5.3.4 PCL PU synthesis and analysis

Optimal degradable polymers for use in skin healing applications should be soft, strong, and elastic. PCL PUs consisting of PCL diol, LTI, and BD were mixed in various ratios (Table 4).

Polymer Code	PLGA-TMP/LTI/BD Molar Ratio
dPU5	1/2/1.5
dPU6	1/2.5/2.25
dPU7	1.5/2/1.5

Table 4. Chemical compositions of PCL PUs

All formulations were found to be elastic and non-brittle. Degradation products of all formulations were found to be non-toxic. All compounds degraded fully in NaOH accelerated conditions, indicating that they would fully degrade via hydrolysis in *in vivo* conditions. Precision-porous scaffolds fabricated from PCL PUs exhibited consistent, uniform pore structure (Fig 26).

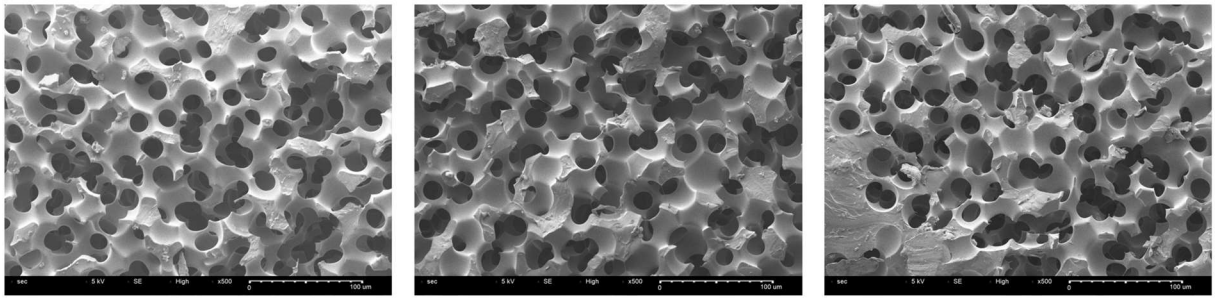

Figure 26. SEM images of PCL PUs at 500x

5.4 Conclusions

Degradable PLGA PUs and PCL PUs were synthesized and tested for degradability and biocompatibility. Polymers composed of PLGA-TMP, BD, and LTI were found to have tunable degradation times in the range of 6-10 weeks *in vitro* and produce non-toxic degradation products. Polymers composed of PCL diol, BD, and LTI were degradable, non-toxic, and suitable for precision-porous scaffold applications.

5.5 Acknowledgements

I would like to acknowledge Felix Simonovsky, PhD. For his guidance on the development of biodegradable PU formulations. I would like to acknowledge Prof. Buddy Ratner for the design of the project and mentorship. Generous funding for this work was provided by a grant from the Northwest Kidney Centers to the University of Washington Center for Dialysis Innovation (CDI)

Chapter 6. REFERENCES

1. Underlying Cause of Death, 2018-2021, Single Race Request Form. https://wonder.cdc.gov/controller/datarequest/D158.

2. Anderson, J. M., Rodriguez, A. & Chang, D. T. Foreign body reaction to biomaterials. *Semin. Immunol.* **20**, 86–100 (2008).

3. von Recum, A. F. Applications and failure modes of percutaneous devices: a review. *J. Biomed. Mater. Res.* **18**, 323–336 (1984).

4. Peramo, A. & Marcelo, C. L. Bioengineering the Skin–Implant Interface: The Use of Regenerative Therapies in Implanted Devices. *Ann Biomed Eng* **38**, 2013–2031 (2010).

5. Underwood, R. A. *et al.* Quantifying the effect of pore size and surface treatment on epidermal incorporation into percutaneously implanted sphere-templated porous biomaterials in mice. *Journal of Biomedical Materials Research Part A* **98A**, 499–508 (2011).

6. Fleckman, P. *et al.* Cutaneous and inflammatory response to long-term percutaneous implants of sphere-templated porous/solid poly(HEMA) and silicone in Mice. *J Biomed Mater Res A* **100**, 1256–1268 (2012).

7. Vojtassák, J. *et al.* Autologous biograft and mesenchymal stem cells in treatment of the diabetic foot. *Neuro Endocrinol Lett* **27 Suppl 2**, 134–137 (2006).

8. Hong, S. J. *et al.* Topically Delivered Adipose Derived Stem Cells Show an Activated-Fibroblast Phenotype and Enhance Granulation Tissue Formation in Skin Wounds. *PLOS ONE* **8**, e55640 (2013).

9. Wu, Y., Chen, L., Scott, P. G. & Tredget, E. E. Mesenchymal Stem Cells Enhance Wound Healing Through Differentiation and Angiogenesis. *Stem Cells* **25**, 2648–2659 (2007).

10. Helena Zomer, Talita Jeremias, Buddy Ratner, & Andrea Trentin. Mesenchymal stromal cells from dermal and adipose tissues induce macrophage polarization to a pro-repair phenotype and improve skin wound healing - ClinicalKey. https://www.clinicalkey.com/#!/content/playContent/1-s2.0-S146532492030058X?returnurl=https:%2F%2Flinkinghub.elsevier.com%2Fretrieve%2Fpii%2FS1465324920300 58X%3Fshowall%3Dtrue&referrer=https:%2F%2Fpubmed.ncbi.nlm.nih.gov%2F.

11. Sullivan, T. P., Eaglstein, W. H., Davis, S. C. & Mertz, P. The Pig as a Model for Human Wound Healing. *Wound Repair and Regeneration* **9**, 66–76 (2001).

12. Sussman, E. M., Halpin, M. C., Muster, J., Moon, R. T. & Ratner, B. D. Porous implants modulate healing and induce shifts in local macrophage polarization in the foreign body reaction. *Ann Biomed Eng* **42**, 1508–1516 (2014).

13. Marshall, A. Biomaterials with tightly controlled poresize that promote vascular in-growth. *Polymer Preprints* **45**, 100–101 (2004).

14. Zhen, L. *et al.* Precision-porous polyurethane elastomers engineered for application in pro-healing vascular grafts: Synthesis, fabrication and detailed biocompatibility assessment. *Biomaterials* **279**, 121174 (2021).

15. Fukano, Y. *et al.* Epidermal and dermal integration into sphere-templated porous poly(2-hydroxyethyl methacrylate) implants in mice. *J Biomed Mater Res A* **94**, 1172–1186 (2010).

16. Brown, B. N., Ratner, B. D., Goodman, S. B., Amar, S. & Badylak, S. F. Macrophage polarization: An opportunity for improved outcomes in biomaterials and regenerative medicine. *Biomaterials* **33**, 3792–3802 (2012).

17. Madden, L. R. *et al.* Proangiogenic scaffolds as functional templates for cardiac tissue engineering. *Proceedings of the National Academy of Sciences* **107**, 15211–15216 (2010).

18. Doppalapudi, S., Jain, A., Khan, W. & Domb, A. J. Biodegradable polymers—an overview. *Polymers for Advanced Technologies* **25**, 427–435 (2014).

19. Zaid, M. B., O'Donnell, R. J., Potter, B. K. & Forsberg, J. A. Orthopaedic Osseointegration: State of the Art. *JAAOS - Journal of the American Academy of Orthopaedic Surgeons* **27**, e977 (2019).

20. Haddadin, Y., Annamaraju, P. & Regunath, H. Central Line–Associated Blood Stream Infections. in *StatPearls* (StatPearls Publishing, Treasure Island (FL), 2023).

21. Read, R. R. *et al.* Peritonitis in peritoneal dialysis: Bacterial colonization by biofilm spread along the catheter surface. *Kidney International* **35**, 614–621 (1989).

22. Arciola, C. R., Campoccia, D. & Montanaro, L. Implant infections: adhesion, biofilm formation and immune evasion. *Nat Rev Microbiol* **16**, 397–409 (2018).

23. Xu, J., Sherry L. Murphy, Kenneth D. Kochanek, & Elizabeth Arias. Mortality in the United States, 2021. *NCHS Data Brief* (2022).

24. Nissenson, A. R. Improving Outcomes for ESRD Patients: Shifting the Quality Paradigm. *Clin J Am Soc Nephrol* **9**, 430–434 (2014).

25. Anderson, J. M. Biological Responses to Materials. *Annu. Rev. Mater. Res.* **31**, 81–110 (2001).

26. Luttikhuizen, D. T., Harmsen, M. C. & Van Luyn, M. J. A. Cellular and molecular dynamics in the foreign body reaction. *Tissue Eng.* **12**, 1955–1970 (2006).

27. Williams, D. F. On the mechanisms of biocompatibility. *Biomaterials* **29**, 2941–2953 (2008).

28. Ward, W. K. A Review of the Foreign-body Response to Subcutaneously-implanted Devices: The Role of Macrophages and Cytokines in Biofouling and Fibrosis. *J Diabetes Sci Technol* **2**, 768–777 (2008).

29. Nilsson, B., Ekdahl, K. N., Mollnes, T. E. & Lambris, J. D. The role of complement in biomaterial-induced inflammation. *Molecular Immunology* **44**, 82–94 (2007).

30. Ratner, B. D. Reducing capsular thickness and enhancing angiogenesis around implant drug release systems. *Journal of Controlled Release* **78**, 211–218 (2002).

31. Veiseh, O. *et al.* Size- and shape-dependent foreign body immune response to materials implanted in rodents and non-human primates. *Nature Materials* **14**, 643–651 (2015).

32. Tang, L. & Eaton, J. W. Fibrin(ogen) mediates acute inflammatory responses to biomaterials. *Journal of Experimental Medicine* **178**, 2147–2156 (1993).

33. Negishi, H. *et al.* Negative regulation of Toll-like-receptor signaling by IRF-4. *Proc Natl Acad Sci U S A* **102**, 15989–15994 (2005).

34. Honma, T. & Hamasaki, T. Ultrastructure of multinucleated giant cell apoptosis in foreign-body granuloma. *Vichows Archiv A Pathol Anat* **428**, 165–176 (1996).

35. Brodbeck, W. G. *et al.* Influence of biomaterial surface chemistry on the apoptosis of adherent cells. *Journal of Biomedical Materials Research* **55**, 661–668 (2001).

36. DiEgidio, P. *et al.* Biomedical implant capsule formation: lessons learned and the road ahead. *Ann Plast Surg* **73**, 451–460 (2014).

37. Klopfleisch, R. & Jung, F. The pathology of the foreign body reaction against biomaterials. *Journal of Biomedical Materials Research Part A* **105**, 927–940 (2017).

38. Ratner, B. D. A pore way to heal and regenerate: 21st century thinking on biocompatibility. *Regen Biomater* **3**, 107–110 (2016).

39. Crawford, L., Wyatt, M., Bryers, J. & Ratner, B. Biocompatibility Evolves: Phenomenology to Toxicology to Regeneration. *Adv Healthc Mater* **10**, e2002153 (2021).

40. Gordon, S. Alternative activation of macrophages. *Nat Rev Immunol* **3**, 23–35 (2003).

41. Mosser, D. M. & Edwards, J. P. Exploring the full spectrum of macrophage activation. *Nature Reviews Immunology* **8**, 958–969 (2008).

42. Linnes, M., Ratner, B. D. & Giachelli, C. M. A FIBRINOGEN BASED PRECISION MICROPOROUS SCAFFOLD FOR TISSUE ENGINEERING. *Biomaterials* **28**, 5298–5306 (2007).

43. Sheikholeslam, M., Wright, M. E. E., Jeschke, M. G. & Amini-Nik, S. Biomaterials for Skin Substitutes. *Advanced Healthcare Materials* **7**, 1700897 (2018).

44. BROWN, B. N. & BADYLAK, S. F. Extracellular matrix as an inductive scaffold for functional tissue reconstruction. *Transl Res* **163**, 268–285 (2014).

45. Weissman, I. L. Stem Cells: Units of Development, Units of Regeneration, and Units in Evolution. *Cell* **100**, 157–168 (2000).

46. Duscher, D. *et al.* Stem Cells in Wound Healing: The Future of Regenerative Medicine? A Mini-Review. *Gerontology* **62**, 216–225 (2015).

47. Nourian Dehkordi, A., Mirahmadi Babaheydari, F., Chehelgerdi, M. & Raeisi Dehkordi, S. Skin tissue engineering: wound healing based on stem-cell-based therapeutic strategies. *Stem Cell Res Ther* **10**, 111 (2019).

48. Guo, X. *et al.* Grafting of mesenchymal stem cell-seeded small intestinal submucosa to repair the deep partial-thickness burns. *Connect Tissue Res* **57**, 388–397 (2016).

49. Pawlaczyk, M., Lelonkiewicz, M. & Wieczorowski, M. Age-dependent biomechanical properties of the skin. *Postepy Dermatol Alergol* **30**, 302–306 (2013).

50. Kuijpers, A. J. *et al.* Cross-linking and characterisation of gelatin matrices for biomedical applications. *Journal of Biomaterials Science, Polymer Edition* **11**, 225–243 (2000).

51. Ashcroft, G. S. *et al.* Estrogen accelerates cutaneous wound healing associated with an increase in TGF-beta1 levels. *Nat Med* **3**, 1209–1215 (1997).

52. Brown, R. C. & Hopps, H. C. Staining of Bacteria in Tissue Sections: A Reliable Gram Stain Method. *American Journal of Clinical Pathology* **60**, 234–240 (1973).

53. Kinney, B. M., Kanakov, D. & Yonkova, P. Histological examination of skin tissue in the porcine animal model after simultaneous and consecutive application of monopolar radiofrequency and targeted pressure energy. *J Cosmet Dermatol* **19**, 93–101 (2020).

54. Masson-Meyers, D. S. *et al.* Experimental models and methods for cutaneous wound healing assessment. *Int J Exp Pathol* **101**, 21–37 (2020).

55. Benjamini, Y. & Yekutieli, D. The control of the false discovery rate in multiple testing under dependency. *The Annals of Statistics* **29**, 1165–1188 (2001).

56. Freihat, L. A. *et al.* IRAK3 modulates downstream innate immune signalling through its guanylate cyclase activity. *Sci Rep* **9**, 15468 (2019).

57. Shen, P. *et al.* IRAK-M alters the polarity of macrophages to facilitate the survival of Mycobacterium tuberculosis. *BMC Microbiol* **17**, 185 (2017).

58. Dai, M. *et al.* CYP2J2 and Its Metabolites EETs Attenuate Insulin Resistance via Regulating Macrophage Polarization in Adipose Tissue. *Sci Rep* **7**, 46743 (2017).

59. Spiller, K. L. *et al.* The role of macrophage phenotype in vascularization of tissue engineering scaffolds. *Biomaterials* **35**, 4477–4488 (2014).

60. Jain, N. & Vogel, V. Spatial confinement downsizes the inflammatory response of macrophages. *Nature Mater* **17**, 1134–1144 (2018).

61. Kim, M. S. *et al.* An in vivo study of the host tissue response to subcutaneous implantation of PLGA- and/or porcine small intestinal submucosa-based scaffolds. *Biomaterials* **28**, 5137–5143 (2007).